Nonlinear Time-Variant Response in an Avalanche Photodiode Array Based Laser Detection and Ranging System

THESIS

Michael D. Seal, Captain, USAF

AFIT/GEO/ENG/07-03

DEPARTMENT OF THE AIR FORCE
AIR UNIVERSITY

AIR FORCE INSTITUTE OF TECHNOLOGY

Wright-Patterson Air Force Base, Ohio

The views expressed in this thesis are those of the author and do not reflect the official policy or position of the United States Air Force, Department of Defense, or the United States Government

AFIT/GEO/ENG/07-03

Nonlinear Time-Variant Response in an Avalanche Photodiode Array Based Laser Detection and Ranging System

THESIS

Presented to the Faculty

Department of Electrical and Computer Engineering

Graduate School of Engineering and Management

Air Force Institute of Technology

Air University

Air Education and Training Command

In Partial Fulfillment of the Requirements for the

Degree of Master of Science in Electrical Engineering

Michael D. Seal, B.S.E.E.

Captain, USAF

March 2007

AFIT/GEO/ENG/07-03

Nonlinear Time-Variant Response in an Avalanche Photodiode Array Based Laser Detection and Ranging System

Michael D. Seal, B.S.E.E.
Captain, USAF

Approved:

/signed/	15 Feb 2007
Steven Cain, PhD (Chairman)	date
/signed/	15 Feb 2007
Michael Marciniak, PhD (Member)	date
/signed/	15 Feb 2007
Richard Richmond (Member)	date

Abstract

This research effort identifies and models the nonlinear time-variant behavior exhibited by an avalanche photodiode (APD) array based laser ranging and detection (LADAR) system. This examination was prompted by the failure of the range accuracy results, in test measurements, to approach the expected Cramer-Rao lower bound for accuracy, and anomylous signal level behavior which was not predicted by the system model.

Based on the original linear time-invariant (LTI) model, the expected evolution of error in the LADAR signal is examined sequentially from the outgoing pulse through signal digitization. This error evolution shows the LTI model does not contain a mechanism for causing the observed signal deviations or to explain the failure of the system to meet the Cramer-Rao lower bound. Therefore, a nonlinear time-variant model is developed based on the interactions of the APDs in the array with the array's voltage regulator.

In the refined model, the sum photo-current for the entire array places a load on a voltage regulator. Given a changing load during the 36 nanosecond range gate, the voltage regulator cannot maintain its output at the reference voltage. The resulting reverse bias voltage variations cause the responsivity of each APD to vary in a nonlinear fashion. Because each APD in the array's responsivity depends upon the entire array's photonic loading, each individual APD's response is time variant. However, if the system's response to photonic loading is incorporated into the model for each detector, ranging algorithms based on linear systems models can be used on the resulting signals.

Acknowledgements

As with most endeavors, which may be judged worthy, a great many thanks are owed to a great many people. In particular, I would like to express my appreciation to my faculty advisor, Dr. Stephen Cain, for his guidance during the thesis process. Thanks are also due to my sponsor, Rich Richmond via the Air Force Research Laboratories, Combat Identification Branch of the Sensors Directorate, for allowing me to tackle one more fascinating problem with my former co-workers. Thanks and apologies must be extended to my wife and brother, who bore the brunt of my thinking aloud regarding my thesis and contributed significantly to the editing of the final document.

Michael D. Seal

Table of Contents

List of Figures

List of Symbols

Symbol		Page
$\mathbf{d_{diff}}$	Diffraction limited blur spot diameter	13
$\mathbf{F}$	APD excess noise factor	15
$\mathbf{G}$	average APD gain	15
$\boldsymbol{\alpha}$	Electron impact ionization coefficient	15
$\boldsymbol{\beta}$	Hole impact ionization coefficient	15
$\mathbf{f_c}$	Maximum transmitted spatial frequency	16
$\boldsymbol{\omega}$	Effective aperture radius	16
$\mathbf{z}$	Aperture to focal plane distance	16
$\boldsymbol{\lambda}$	Wavelength	16
$\mathbf{q}$	Pixel row index	18
$\mathbf{r}$	Pixel column index	18
$\mathbf{k}$	Range position in the range gate	18
$\mathbf{p_w}$	APD excess noise factor	19
$\mathbf{c}$	The speed of light in a vacuum	19
$\mathbf{V_{BD}}$	Reverse breakdown voltage	23
$\mathbf{V_{Bias}}$	Reverse Bias Voltage	23
$\mathbf{p}$	Empirical Scaling Factor	23
$\mathbf{V_{ref}}$	Voltage Regulator Reference Voltage	39
$\mathbf{V_D}$	Voltage Regulator Deviation Voltage	39
$\mathbf{x}$	LCCDE input value	40
$\mathbf{y}$	LCCDE output value	40
$\mathbf{k}$	Discrete Time Index	43

List of Abbreviations

Abbreviation		Page
LADAR	LAser Detection and Ranging	1
FOV	Field of View	2
AFRL	Air Force Research Laboratories	2
SNJM	Sensors Directorate, Electro-Optic Combat ID Branch	2
ASC	Advanced Scientific Concepts, Inc.	2
IFOV	Instantaneous Field of View	2
APD	Avalanche Photodiode	3
ROIC	Read-Out Integrated Circuit	3
FPA	Focal Plane Array	5
PSF	Point Spread Function	13
NUC	Non-Uniformity Correction	15
GWAN	Gaussian White Additive Noise	17
MSE	Mean Squared Error	19
RGB	Range-Gain-Bias	19
LTI	Linear Time Invariant	20
PID	Proportional Integral Derivative	22
RC	Resistive-Capacitive	22
LCCDE	Linear Constant-Coefficient Difference Equation	40

Nonlinear Time-Variant Response in an Avalanche Photodiode Array Based Laser Detection and Ranging System

I. Introduction

1.1 Laser Radar Applications

Advances in airpower have assured the future of laser radar on the modern battlefield. In the absence of air superiority, an army will find that any vehicle, structure, or even troop concentration, which can be located, can be destroyed. Thus, camouflage and deception have taken on a key position in military operations. Keeping pace with these developments, modern camouflage extends beyond the familiar visual camouflage patterns which break up the outlines of personnel and equipment. It has evolved into full signature management systems, addressing how the camouflage matches its intended environment in the visible, infrared, and radar regimes [14]. Laser Detection and Ranging (LADAR) is a method, under continuing development, for defeating this type of camouflage.

Currently fielded optical sensor systems primarily rely upon their spatial resolution to locate and identify targets. An operator examines an image with finite resolution collected by systems such as low light cameras, photomultiplier based passive night vision devices, or forward looking infrared systems to identify targets. While these systems may provide magnification and extend the portion of the electromagnetic spectrum the operator can view, the images are still interpreted by the operator for target recognition. Therefore, classical techniques to deceive operators attempt to make the image of the object appear to be something else or to cause insufficient contrast between the target and its background for detection.

LADAR may be exploited to overcome both methods of deception. First, by adding range information to the image, the three dimensional shape of objects can

be determined regardless of the intensity image mapped over its surface. Even if the exact image of the terrain behind it were displayed on the imaged side of a target, its range profile will stand out from the true background. If the material used to mask or break up the target's signature does not cover it completely, as is often the case with camouflage netting, there will be gaps through which the target can be viewed [14]. LADAR systems capable of detecting multiple returns can form multiple layer range profiles showing both the camouflage and what is underneath it.

To be effective on the modern battlefield, a LADAR system must be able to quickly and accurately make range measurements on its entire field of view (FOV). As with all measurement devices, random and systematic error is introduced into the results. While typically random errors can only be suppressed, systematic errors can be removed from a well-modeled system. The objective of this work is to identify and delineate the random from the systematic errors in the range data generated by an experimental FLASH LADAR, and to develop a model which can be used to remove the systematic errors.

1.2 AFRL/SNJM FLASH LADAR Specifications

The imaging angle-angle-range LADAR operated by the Electro-Optic Combat Identification Branch of the Air Force Research Laboratories' Sensors Directorate (AFRL/SNJM) is a FLASH LADAR system from Advanced Scientific Concepts (ASC) mated with a 1.55-μm Big Sky CFR-400 laser. In angle-angle-range format, as in a digital camera, a common optical system forms an image on an array of individual detectors or pixels arranged in a grid pattern. Consequently, each pixel is exposed to an instantaneous field of view (IFOV) spanning some finite vertical and horizontal angle within the FOV of the entire system.

Range data is found by illuminating the target area with a laser pulse and delaying data capture to collect the returning pulse. The irradiance on each pixel in the array is then recorded at a 1.862-nanosecond sampling period to form a series of nineteen images over approximately 35 nanoseconds. The time series of irradiance

values recorded by each pixel is processed to determine a range for the object or objects within its IFOV.

The most novel component of the FLASH LADAR system is an avalanche photodiode (APD) array fabricated by Sensors Unlimited Inc. which is mated to an ASC Read-Out Integrated Circuit (ROIC). The detector array is 128 x 128 pixels, representing a significant advance in indium gallium arsenide APD array fabrication at the time of its development. Due to the guard ring structure of each APD, the active detector area is approximately 40-μm x 40-μm with detectors on 100-μm centers. Immersion lenses are used to increase the effective fill factor of the detector array to near 100 percent, significantly increasing the flux collecting efficiency of the receiver [17].

The FLASH LADAR has two modes for sampling the period in which the laser pulse actually returns to the detector. In stop mode, a buffer is cyclically filled and overwritten for several samples after any pixel crosses an irradiance threshold. Thus, the range to the target need not be guessed to determine when to stop overwriting the buffer. In sular mode, a software selected range gate is selected to delay write-out until a returning pulse from the selected range is expected to arrive. Both modes result in an output record in which the first image written out is not necessarily the first in the true time sequence. This is simply rectified by reordering the images after the buffer stop time to be first, and then appending any leading images to the end of the record [17].

The sular operating mode was used almost exclusively for collecting data sets for algorithm development. In this mode, the range gate consistently observes the same area, so multiple frames can be averaged to reduce noise. The measurement consistency also led to the development of a direct method for removing ambient light and fixed pattern noise. This method consisted of subtracting a frame of data taken in sular mode with the laser inactive from frames taken with the laser active.

A system model was derived for the FLASH LADAR, incorporating a series of assumptions, which are typical of cameras and infrared imagers. First, each detector

was considered to be a completely independent device comprised of an APD, capacitor bank, amplifier, and analog-to-digital conversion circuitry. Second, each device has a characteristic average responsivity, due to the APD responsivity and amplifier, and there is some variation in responsivity between devices. Third, each detector is capable of collecting and digitizing the photonic signals of interest with negligible impulse response effects. This model, for a single detector, is shown in Figure 1.1.

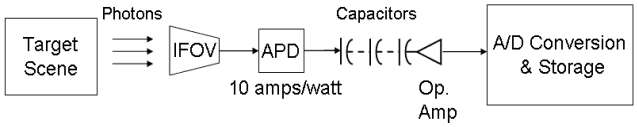

Figure 1.1: Original system model

1.3 Design Impact on System Performance

The FLASH LADAR system was designed to meet a series of design requirements. Chief among these was a high a responsivity which peaked in the near infrared region. A high, for a developmental device, spatial resolution was also required.

Imaging arrays of APDs are significant for laser radar applications because they have greater than unity detector gain. The gain is derived from one incident photon generating many electrons in the detector material, and allows for detector responsivities as high as 10 Amps/Watt at the design wavelength of the APD array [2]. A high responsivity is critical for laser radars examining distant targets, because very few

photons will be collected by the imaging optics. Alternatively, this high responsivity can be exploited to allow eye-safe experimentation on nearby targets.

While a high responsivity improves the signal to noise ratio of the LADAR return, the type of ranging algorithms which produces the most accurate results depends strongly on the system resolution trade offs. For a given system, the highest possible spatial and range resolution for a given system is desirable, but any realizable system will always have some total sample count limitation per range image. This limit may arise from repetition rate requirements or the limitations of focal plane array FPA and ROIC fabrication technologies. In the case of the FLASH LADAR, the FPA was fabricated with 128x128 detectors and the ROIC with 19 integrating capacitors switching at a fabrication limit.

Khourey *et al.* defines a voxel as the volume enclosed by the sample spacing across the image plane and in range. It is common to design a system to achieve a nearly cubic voxel at a design range, for instance one cubic meter at ten kilometers [7]. In this case, with an f/2 lens system, the sampled voxel is approximately 1" by 1" by 1.5' at a typical target range of approximately 80 yards. Consequently, the data collected for algorithm development has much more spatial resolution than range resolution, due to sampling. Therefore, early algorithmic work focused on algorithms capable of making sub-sample accuracy range determinations.

1.4 Initial Research Results

Initial research emphasized target sets for which the results were readily predicted by the system model. One of the first test was conducted on a two surface target board set shown in Figure 1.2. Since both target surfaces are retroreflecting, the returning signals from them are expected to be delayed and attenuated versions of the outgoing pulse shape, with additional constant valued contributions from the ambient light and dark current. The return from any off target pixel is expected to consist of the ambient light and dark current, as well as a small contribution from

atmospheric backscatter of the laser pulse. An unmodified example of the expected first and second target surface returns at the receiver is shown in Figure 1.3.

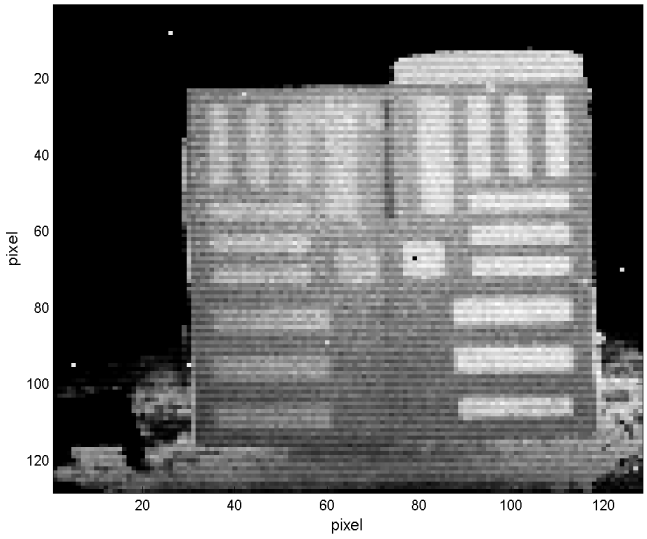

Figure 1.2: Two surface retroreflecting target

These signals are conditioned by a background subtraction scheme, in which an ambient light illuminated record is subtracted from a pulse illuminated record. An ambient light response is taken by disabling the laser output and recording the system response at the same range delay as the pulse illuminated response. Subtracting the ambient light illuminated signal was expected to remove both the photonic contributions due to ambient light, and the dark current response of the system. The expected final results are shown in Figure 1.4

The first sub-range sample accuracy algorithm tests on this target resulted in the two surfaces, which were 40" apart, being measured to be 44" apart. This result was a significantly less accurate measurement than was expected for the algorithm being tested, which was based on a linear time-invariant system model and postulated return pulse shape [1]. While examining these results, it was noted that the recorded signals did not match the signals predicted by the system model. The recorded returns are displayed in Figure 1.5.

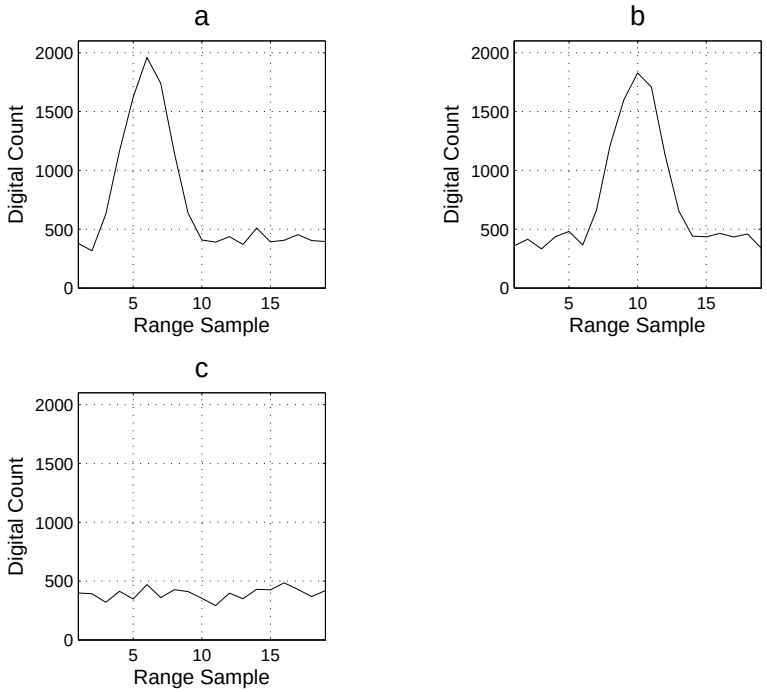

Figure 1.3: a. First surface return b. Second surface return c. Off target

While it appears that there are two returns in each of pulse illuminated returns, this cannot be the case. The targets in the IFOV of the pixels shown are retroreflecting. This indicates that the observed behavior may be some form of system response ringing. Upon close inspection, it can also be seen that the appearant pulse widths are different, between the first and second surfaces. Once again, this cannot be the case for a pair of retroreflecting surfaces. Finally, the behavior of the off target pixel deviates severely from the expected system response. Any response due to atmospheric backscatter must begin as the laser pulse leaves the aperture, and will be a nearly linear response when measured at a significant distant from the aperture, over the range gate.

An additional data set under consideration consists of the same target board set, in a much more range diverse scene. In this case, the first surface of the target represents the start of a broader set of range returns including the second surface, personnel, and foliage. Figure 1.6 subplot a. shows the pulse shape recorded for the first surface of the target board. This pulse exhibits a broader shape than expected,

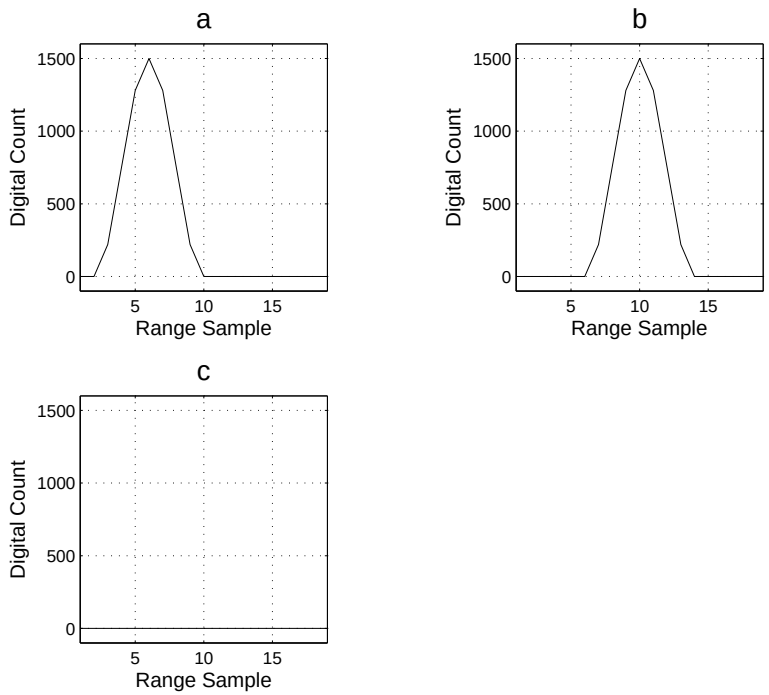

Figure 1.4: a. First surface return b. Second surface return c. Off target

and what may be the start of the anomylous ringing behavior. In the off target pixel response in Figure 1.6 subplot b., a high negative correlation can be seen between the value after background subtraction and the pulse shape from the first surface. This response is distinctly different from the ambient response value, after dark current subtraction, shown in Figure 1.6 subplot c.

This anomylous behavior has several significant implications on the military application of this LADAR system. The observed behavior makes multiple object ranging inside an IFOV impossible. Any multiple surface ranging algorithm would assign two distinct ranges to the recorded data in Figure 1.5, even though a second surface is known to be absent. In general, ranging algorithms would also assign a range to the off target pixels, most likely near the twelfth sample in Figure 1.5. However, the effects of these behaviors on the accuracy of single surface ranging was uncertain.

In an effort to develop a better expectation of the system and algorithm's analytical measurement accuracy, the Cramer-Rao lower bound was calculated for the

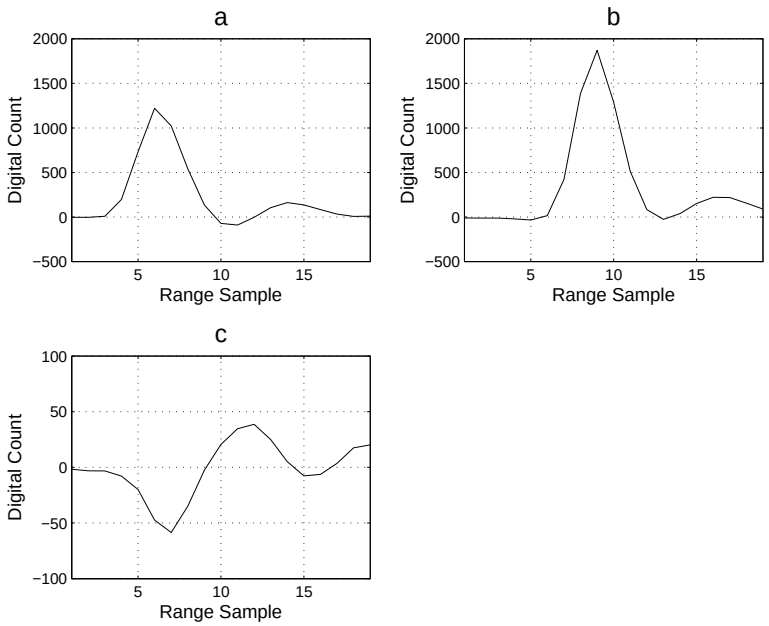

Figure 1.5: Pulsed values minus background a. First surface return b. Second surface return c. Off target return

sub-range sample accuracy algorithm under consideration, given a single-surface test case. For this case, the bound was found to be approximately 3/5". However, this result is for an unbiased estimator and the ranging algorithm does not meet this requirement for returns exhibiting the observed anomylous behavior [16]. In practice, the FLASH LADAR range accuracy for the algorithm and test case was found to be 2.5". Therefore, the next major research objective is to identify the source of and model the anomylous signal behavior, and implement the resulting model into ranging algorithms.

1.5 Research Scope

The primary objective of this work is to investigate and model the anomylous signal behavior of the FLASH LADAR under optical loading. A refined system level model is proposed, based upon key system elements for which partial models or descriptions are available. Due to the lack of an appropriately controlled test case, only a forward model is developed. Although the detailed analysis to follow is specific to

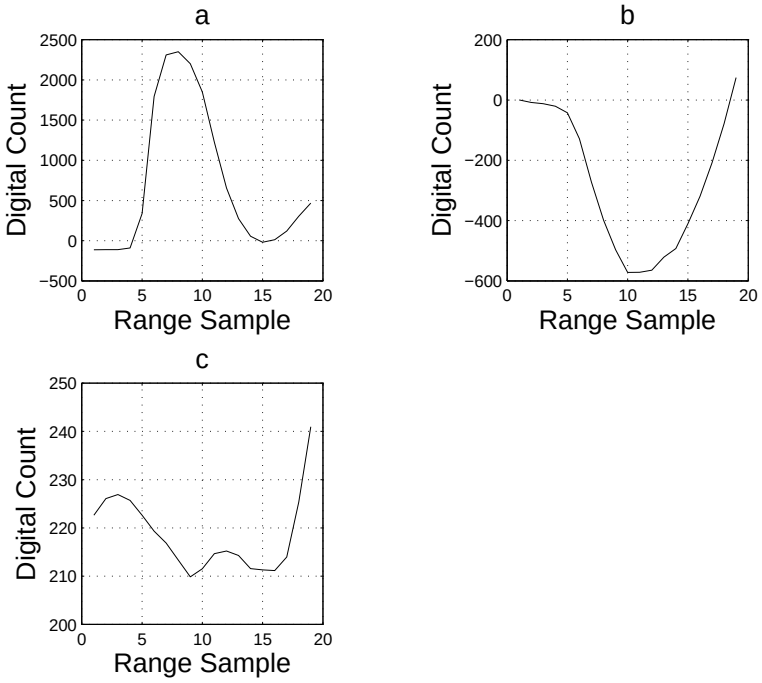

Figure 1.6: a. First surface after background subtraction b. Off target pixel after background subtraction c. off target ambient response minus dark response

the FLASH LADAR, the general principles of the model are applicable to any APD array based LADAR, of similar design.

1.6 Research Methodology

The type and scope of investigations which can be carried out to address this problem are, by necessity, limited. The functionality of the LADAR system cannot be compromised, so partial disassembly for component measurements is not possible. There is also a limited amount of published information regarding detailed system specifications, due to intellectual property and security requirements. Consequently, the system is treated in a gray-box manner, with limited known parameters.

The analytical approach which follows was used to identify the deviations between the modeled and recorded system responses, and develop a refined model. First, the original system's error model is presented following the laser pulse from transmission to and from the target, through the optical system, into the detection and

digitization process, and finally through range interrogation by various algorithms. This signal error evolution accounts for deviations due to known sources, in their generally accepted forms. Then, a hypothetical system model is proposed to explain the anomylous behavior. Beginning with the digitized output of the system, the detection process is reversed to examine the system behavior, and develop a predictive forward model for the system. The forward model is completed by solving a system of linear constant-coefficient difference equations to identify the remaining linear system behavior. Finally, the proposed forward model is compared to a recorded case for validation.

II. Background

2.1 Introduction

The objective of the FLASH LADAR system is to assign a range to each pixel by evaluating a recorded pulse return with a ranging algorithm. It was presumed, in the original model, that the LADAR system's response was both linear time-invariant and had negligible effects on the recorded pulse shape. The performance of any ranging algorithm is degraded by random noise, and all ranging algorithms incorporate a series of assumptions about the signal being processed. If the noise level is too high or the assumptions are in error, the Cramer-Rao limit for ranging accuracy cannot be achieved. Therefore, the expected evolution of error in the FLASH LADAR model is examined to account for known systematic and random effects. Then, a series of common ranging algorithms and their associated assumptions are presented and compared to the behavior of the recorded signals.

2.2 Signal Error Evolution

The ideal return signal for the FLASH LADAR is the convolution of a linearly scaled version of a known outgoing laser pulse shape with a single retro-reflecting surface in each pixel's IFOV [18]. The resulting return is an attenuated copy of the outgoing laser pulse recorded some time after the pulse was transmitted. However, numerous factors cause the recorded return to deviate from this ideal state: random error is introduced by the lasing process; the atmosphere between the FLASH LADAR and target surfaces; the photonic detection process, and the digitization process. Systemic errors are also introduced by the range profile of the target within each pixel's IFOV, the system's optical train, the detector array, and the digitization process. These sources of error will be examined following the system's signal path from the outgoing laser pulse to the reported digital output.

2.2.1 Transmitted Pulse. A well-characterized laser source is a critical first component of any LADAR system, because all ranging methods require some knowl-

edge of the transmitted pulse shape. While well-behaved pulses can be consistently generated, there will always be some random error between the designed and the actual individual outgoing pulse shape. When ranging algorithms are applied, any deviation from the expected pulse shape in a LADAR return will eventually manifest itself as a range estimation error. Even the mathematically ideal returning pulse shape can introduce error in deconvolution, if more than one range is represented in a pixel's IFOV [18].

The transmitted pulse must be of sufficient power that a detectable number of photons will be scattered back towards the LADAR from the target being illuminated. Additional power, beyond the device minimum for detetion, is required because the signal entering the detector will not consist solely of the laser pulse energy reflected from the target. It will also include in-band photons from other sources such as self emission or solar reflection [9]. The pulse must contain sufficient power to achieve at least a signal-to-noise ratio of one with these sources, upon arrival at the detector.

The atmosphere, through which the laser pulse travels, affects the laser pulse traveling both to and from the target. Scattering and absorption in the atmosphere attenuate the returning pulse by reducing the number of photons which return to the FLASH LADAR. Speckle noise, which arises from the coherence of the laser pulse, also causes error in the returning signal. The end result of speckle noise is to cause random deviations in the flux distribution collected at the receiver, due to interference [4].

2.2.2 Optical Train. The first systematic error introduced by the receiver is due to the optical system's point spread function (PSF). For perfect optics, the PSF is governed by diffraction through the finite aperture of the system's entrance pupil. The image formed by the optical system is the convolution of the PSF with the flux distribution on the system's entrance pupil. The normal result, for physical systems, is to introduce light from a point source onto a finite area.

Assuming diffraction limited performance, the f/2 lens system used is expected to yield a diffraction blur spot diameter $\mathbf{d_{diff}}$ of 7.564-μm according to the relationship

expressed in equation (2.1) [3]. For the discretely sampled image plane of the LADAR, the key deviation arises from a portion of the irradiance which was expected to fall on a certain pixel instead falling on multiple nearby pixels. Therefore, if uncorrected, the irradiance record on each pixel will contain information from outside its IFOV [5].

$$d_{diff} = 2.44 * \lambda * \mathrm{f}/\# \tag{2.1}$$

Any realizable lens system also introduces aberrations in the image. The laser source means that the light of interest entering the system is quasi-monochromatic, and the primary aberrations will be the Seidel aberrations [6]. For the purposes of ranging, the most harmful of effect spherical aberration, coma and astigmatism is to blur the image by introducing light from outside each pixel's IFOV. Petzval field curvature and distortion also redistribute the light from the target. If the image is properly sampled, these aberrations spatially misplace the resulting range from its true location on the object, but may not introduce ambiguity in the ranging process [6].

The average PSF can be accurately measured, and the aberrations minimized and measured for an optical train. This is particularly straight forward for systems such as LADARs, which are nearly monochromatic [6]. For well-characterized systems, these effects can be deconvolved from the data if the minimum sampling requirements are met and random noise can be addressed effectively [5].

2.2.3 Photonic and Detector Noise. Photonic detection is a random arrival process, which is well studied for the system under consideration [4]. The pulse returns from a coherently illuminated scene onto a detector with a sampling area which is much larger than a coherence area on the detector. Therefore, the arrival process takes on a negative binomial form dependent upon the average photon count and speckle parameter [16]. The system operates at f/2, with a center wavelength of 1.55-μm, and a detector size of 100-μm x 100-μm. This yields a speckle cell width of approximately 3-μm, and a detector area to speckle cell area ratio of 178 to 1. This

ratio is the speckle parameter. For speckle parameters much greater than one, such as this case, the arrival distribution approaches a Poisson distribution [16].

The detectors in the FLASH LADAR are avalanche photodiodes. APDs have a non-unity internal gain term which multiplies shot and photonic noise along with the signal, and introduces its own excess noise term as defined in equation (2.2). This excess noise term, **F**, stems from the statistical nature of the gain term, and is mathematically expressed as a function of the average gain, **G**, the electron impact ionization coefficient, $\boldsymbol{\alpha}$, and the hole impact ionization coefficient, $\boldsymbol{\beta}$ [3]. The excess noise factor typically begins to dominate other noise sources, including read-out noise, above gains of twenty. It is not expected to be the dominant noise source for this system, which has a gain of approximately ten.

$$F = \frac{\beta}{\alpha}G + \left(1 - \frac{\beta}{\alpha}\right)\left(2 - \frac{1}{G}\right) \tag{2.2}$$

Ideally, if each detector in the array were exposed to the same incident flux, it would report the same averaged photo-electron count. In reality, each APD in the array has its own average gain term and dark current. For constant operating conditions, these terms are dependent upon the physical parameters of each device.

When exposed to a common input flux and allowed to reach a steady-state value, the multiplicative effect of each device's gain and the additive effect of its dark current can be divided and subtracted out to produce a common photo-electron count. The terms necessary for this normalization can then be recorded for each pixel, as a correction factor. This type of correction is typically termed non-uniformity correction (NUC) and is conducted on the final digital output of the device to remove the combined deviations of the detector, amplifier, and sampling circuitry [9].

2.2.4 Sampling in Space and Range. The detector of an angle-angle-range LADAR must sample intensities in both dimensions of the image plane and in range. The Nyquist sampling requirement must be met in each dimension to form an un-

aliased signal at the designed resolution. The factors determining the Nyquist sample rate are quite different between the image plane and in range.

Across the image plane, the signal is truly band-limited due to the system's entrance pupil, and the signal can be sampled at a finite rate with no aliasing. For a single wavelength, the highest spatial frequency, $\mathbf{f_c}$, which is passed by the optical train can be calculated via equation (2.3). In this equation, $\boldsymbol{\omega}$ is the effective aperture radius, $\mathbf{z}$, is the distance from the aperture to the focal plane, and $\boldsymbol{\lambda}$ is the wavelength under consideration.

The FLASH LADAR uses an f/2 lens with a 10-cm entrance pupil. Therefore, the highest spatial frequency which is passed by the optical system is $f_c = 1.613 * 10^5$ m^{-1}. This requires a Nyquist sampling rate of $2 * f_c$ which corresponds to a spacing of 3.1-μm. The system is sampled at 100-μm spacing, and is thus spatially undersampled. Consequently, all of the information recorded by the detector array exhibits spatial aliasing.

$$f_c = \frac{\omega}{\lambda z} \tag{2.3}$$

In range, the pulse shape defines the Nyquist sampling requirement and thus the signal is never truly band-limited. As always when sampling a non-band limited signal, some noise is introduced due to aliasing. Typically, the aliasing noise is mitigated by low pass filtering the signal prior to digitization. In this case, the smoothly varying pulse shape provides significant high-frequency attenuation, reducing the aliasing effect. Additionally, any realizable optical detector applies a low-pass filtering operation to the incident signal, due to the finite detector integration time [5]. For this system, the actual integration time of the detector is not known explicitly, although it is necessarily shorter than the switching time of 1.862 nanoseconds. Based on these factors, the noise due to aliasing in range is assumed to be negligible when compared to other noise sources for this system.

2.2.5 Read-Out and Digitization. In the temporal sampling process, each detector sequentially charges twenty integrating capacitors. At the completion of the overwriting cycle, the charge in the capacitors is read out via an amplifier and undergoes an analog-to-digital conversion process. This process introduces read-out noise based on charge deviation, individual amplifier gain variation, individual amplifier additive offsets, injected amplifier noise, and the rounding process associated with digitization. The random error introduced during read out is typically modeled as Gaussian White Additive Noise, GWAN, while the variation between sets of detector circuitry is represented by an array of multiplicative and additive terms. Both of these types of error enter the final digital count stored by the LADAR, which is significantly rescaled in comparison to a true photo-electron count unless the system is calibrated against a known photonic source.

2.3 Range Determination

An ever-increasing number of methods for deriving range estimates from LADAR returns are available. Most of these methods are fundamentally deconvolution methods with different means of addressing uncertainty in the target shape and noise. Four common methods which will be examined include peak detection, matched filtering, Richardson-Lucy deconvolution, and an estimation-theory-based method [18].

2.3.1 Peak Detection. The simplest method of range estimation is peak detection. Peak detection algorithms are best matched with pulses shorter than the sampling time of the system, but can be applied to longer pulsed systems. This method's range accuracy is directly defined by the clock sampling time, since the peak irradiance value will always be localized in a single time increment. If the returning pulse is temporarily recorded, a clock is started when the pulse is fired. Then, when the irradiance on the detector crosses a preset threshold, the clock is stopped. The resulting round trip time is converted to a round trip distance, assuming the speed of light in a vacuum. If data is recorded shortly before and after the stop time, multiple

threshold crossings can be evaluated. In this way, multiple reflections in the field of view can be ranged rather than only the first [18].

Peak detection provides consistent results in the presence of noise, but provides the least accurate range estimation of all the methods compared in this section. Using peak detection, the FLASH LADAR system has a range uncertainty of approximately 1.5', which is acceptable for weapons ranging, but does not provide the detail necessary for LADAR based target identification [16].

2.3.2 Matched Filtering. In matched filter detection, which is commonly used in radar processing, a noisy or deformed input signal is processed by a filter whose impulse response is the time reverse of the signal to be detected. The peak of the resulting filtered waveform represents the point in time at which the highest correlation was achieved [10]. The mathematical implementation of this system is very fast, but multiple returns in the same signal and other deviations from the expected return shape significantly impact the accuracy of this method. Any additional signal content shifts the position of highest correlation, and thus the range estimate, towards the deviation signal's range. Random noise is expressed by correlation peak broadening and results in ambiguity in the range estimate.

2.3.3 Richardson-Lucy Deconvolution. Many current deconvolution algorithms are based on the iterative Richardson-Lucy algorithm. As such, deconvolution begins by numerically estimating the probability density function of an observed waveform, $o(q, r, k)$, using each sample from each pixel position defined by $\mathbf{q}$ and $\mathbf{r}$ with a range return centered at $\mathbf{k}$. The intensity value in each time increment $d(q, r, k)$ is assumed to be a realization of a random variable, $D(q, r, k)$, with a probability density function based on a noise model appropriate for the system. Bayes Rule indicates the relationship between the as-yet-unknown probability of the actual waveform conditioned on the observed waveform, the probability of the observed waveform, and the probability of the observed waveform conditioned on the actual waveform. This relationship is shown in Equation (2.4).

$$f_{O|D}(o|\, D) = \frac{f_{D|O}(d|\, o)}{f_D(d)} \tag{2.4}$$

A log likelihood estimator for $o(q, r, k)$ then takes the form of Equation (2.5).

$$L(o) = ln(f_{D|O}(d|\, o)) \tag{2.5}$$

The likelihood estimator is then expanded into terms determined by the system model, differentiated, and set equal to zero. An iterative updating solution is used to solve the resulting intractable equation for $o(q, r, k_{new})$ [15]. The solution of the equation, $o(q, r, k_{new})$, is a representation of a noisy range return for the pixel of interest at a given range, k_{new}. If the estimated noise probability distribution function does not represent the actual noise distribution properly, this method may converge on a false range or fail to converge at all. This method responds to bias deviations in a similar manner to matched filter detection.

2.3.4 Range Gain and Bias Estimation. Estimation theory methods attempt to directly fit a scaled and shifted version of the output pulse to the recorded data and iteratively locate the pulse position giving the least-mean-squared error (MSE). This type of algorithm requires searching through all pulse locations under consideration and is more time intensive than other implementations, but can estimate object ranges outside the sampled window and multiple return locations. The range-gain-bias (RGB) estimation method derived by Burris [1], uses a three term model based on an inverted parabola pulse shape with an initially unknown gain, location, or bias level. The pulse model, $I(t_k, x_n, y_m)$, is shown in Equation (2.6).

The gain term, $G(x_n, y_m)$, scales the pulse-shape model, which is truncated by a shifted rectangle function, $rect(f(t_k))$, with a pulse half-width, $\mathbf{p_w}$, in seconds multiplied by the speed of light, $\mathbf{c}$, to preclude negative pulse values. Noise in each voxel is modeled by the $q(t_k, x_n, y_m)$ function. An average bias, $B(x_n, y_m)$, is estimated for

each test location by using the mean of all of the sampled data outside the postulated pulse. Both the gain and bias terms are solved using an estimated range

$$I(t_k, x_n, y_m) = G(x_n, y_m)\left(1 - \frac{(R(x_n,yn) - t_k c)^2}{(cp_w^2)}\right) rect\left(\frac{R(x_n,y_m) - t_k c}{2cp_w}\right) ...$$

$$... + B(x_n, y_m) + q(t_k, x_n, y_m) \tag{2.6}$$

Bias level averaging makes this method tolerant of signal deviations outside the returning pulse, so long as the actual return pulse has higher amplitude than any deviation [1]. If the signal deviates during the pulse, the shape of the pulse and the resulting range estimate will be skewed. Random noise introduces ambiguity in the pulse shape, and thus the range estimate.

2.4 Signal Error and Ranging Summary

Throughout the course of its transit, the LADAR signal has deviated significantly from its desired form. Random error has entered from the laser pulse generation process, atmospheric speckle, photonic arrival, APD gain noise, and read-out noise. The signal has also been systematically deformed by the target's range profile in the IFOV, the optical system's PSF and aberrations, detector non-uniformity, and read-out amplifier non-uniformity. These error sources are intrinsic to the device, and must be dealt with by the ranging algorithms to produce an accurate range estimate.

Ranging methods including peak detection, matched filtering, Richardson-Lucy deconvolution, and a Range-Gain-Bias estimation method were examined. Since all four methods are fundamentally deconvolution methods, a linear time invariant (LTI) model for the recorded signals was intrinsically assumed.

In their generally accepted forms, none of the error sources or ranging models explain the anomylous signal behavior observed. However, the signal flow and LTI requirements for accurate ranging provide an insight into a refined system model which can explain the anomylous behavior and ranging errors.

III. System Model

3.1 Model Hypothesis

Based on observations from Figure 1.5 and Figure 1.6 and the results of the evolution of error analysis, all of the assumptions indicated by the original system model may be erronious. First, the ringing response and pulse width variation observed in Figure 1.5 indicate a non-negligible detector impulse response. For the original model, a non-negligible impulse response indicates that the APD and amplifier responsivities are not constant valued between samples in the record. Thus, the required NUC coefficients are effectively changing during the record and introducing a systematic error. Finally, the correlation between devices which have no common photonic input means that the detectors in the array are not independent. Based on this hypothesis, a refined model of the system is presented.

3.2 Proposed System Model

The following system model is presented to indicate the relationship between the key components of the system, as they relate to the APD gain. The model provides a framework for determining the system behavior, which results in gain variation. It also assigns the time dependence and nonlinearity exhibited by the system to distinct components, so these factors can be removed and the residual system identification problem solved.

A proposed functional model of the system can be seen in Figure 3.1. The photons incident on each pixel are multiplied by a gain term to yield a number of electrons, which flow as current to the integrating capacitors of the ROIC [17]. The sum of each pixel's current demand is fed back to the voltage regulator to produce the bias voltage which drives the APD gain equation shown in Equation (3.1). The charge stored in the integrating capacitors is resistively converted to voltage and passed to an analog-to-digital converter to produce the digital photo-counts which are stored in the system's memory.

$$G = \frac{1}{1 - \left(\frac{V_{Bias}}{V_{BD}}\right)^{p}} \tag{3.1}$$

The configuration of these components suggests that a parameterized model of the system could be developed, but some information is missing. While the voltage regulator is expected to be a closed loop control device of the proportional integral derivative (PID) type, its system parameters are unknown. The network through which the current demand is converted back to a reference voltage for the voltage regulator is also unknown, but assumed to be a resistive-capacitive (RC) rather than purely resistive network [8]. Additional uncertainty is added by the RC network of the integrating capacitors and analog-to-digital converters, since the only data available is the output recorded by the system after analog-to-digital conversion. Models for the APD gain, voltage regulation process, and ROIC are presented in greater detail in sections 3.3, 3.4, and 3.5.

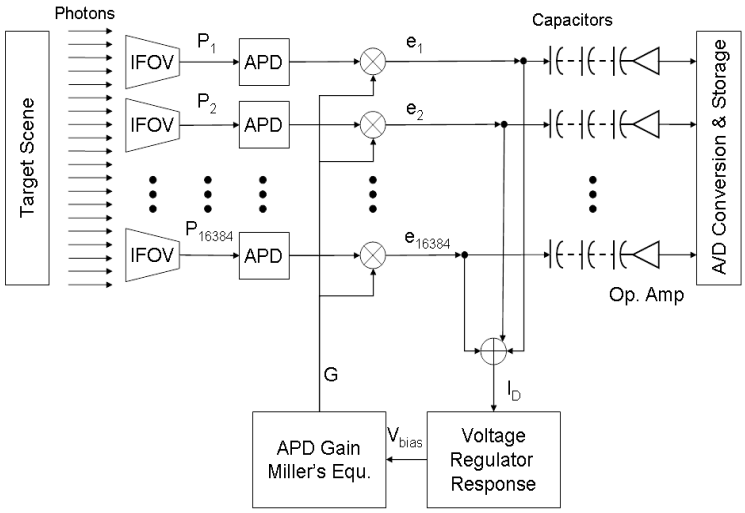

Figure 3.1: Proposed system model diagram

3.3 APD Model Details

Fundamentally, an InGaAs APD is a highly reverse biased PN junction, which is approximately thirty percent quantum efficient. When a photon, of the correct wavelength, is incident on the junction an electron-hole pair is excited out of the depletion region. The strong reverse bias causes these carriers to accelerate and gain enough kinetic energy to excite new carriers by impact ionization as they leave the depletion region. These additional carriers, which are generated from one photon, constitute the APD gain. The number of carriers generated depends on the physical parameters of the device affecting the carrier extinction ratios and on the reverse bias voltage applied across the diode [3]. The empirically derived Miller's Equation is used to directly relate the APD gain to the applied reverse bias voltage, .

Miller's Equation, shown in equation (3.1), indicates that the average gain, $\mathbf{G}$, is a function of the reverse breakdown voltage, $\mathbf{V_{BD}}$, the reverse biasing voltage, $\mathbf{V_{Bias}}$, and an empirical scaling factor, $\mathbf{p}$. The reverse breakdown voltage is a physical parameter of the device, although it can vary with temperature [19]. The scaling factor is found by solving equation (3.1) for $\mathbf{p}$ using known values for the voltages and gain. In this case, equation (3.1) yields a scaling factor value of 5.48. The results of equation (3.2) can then be used to determine the gain resulting from a given reverse bias and breakdown voltage.

$$G = \frac{1}{1 - \left(\frac{V_{Bias}}{V_{BD}}\right)^{p}} \tag{3.2}$$

3.4 Voltage Regulator Model Details

The reverse bias voltage is provided to all of the APDs in the array by a single fast transient response voltage regulator. This device can be simply viewed as a current controlled voltage device. It provides a stable output voltage, when a stable current demand is placed on it. However, when the current demand varies, the device has a transient response during which the voltage will not be maintained at its set

level [12]. For the FLASH LADAR, the current demand on the voltage regulator varies with the photocurrent of the entire array, since all of the APDs are biased by the same regulator.

The following example is given as justification for modeling a variable voltage regulator output. The published dark current for one pixel of a developmental version of the device is 14.4-nA [2]. Under constant dark conditions, the current load required by the entire array would be 16384 times this amount, or 0.236 mA. If a scene were illuminated by a pulse from the specified Big Sky CFR-400 laser, which outputs 7 mJ of energy per pulse, the current demand must increase during the pulse return.

The radiometric calculations required to determine the photonic input to the system for a test board 80-m away progress in the following manner. The vertical and horizontal half angle FOV for an f/2 lens, with a 6.4-mm wide detector, is 32-milliradians. At 80-m this corresponds to viewing an area 5.122-m x 5.122-m. In the data set available for analysis, the target board is centered in the FOV and covers a 2.43-m x 2.43-m square area.

Presuming the laser was focused such that the designed FOV was covered by the first two standard deviations of the pulse's spatial Gaussian distribution, 43-percent of the transmitted flux is incident on the target board. The white board is presumed nominally 10-percent reflective and Lambertian, so the 10-cm collecting optic of the receiver collects only $6.71 * 10^{-7}$-percent of the transmitted pulse or 4.7-nJ. For this example, the APD gain is temporarily assumed to be constant at a value of 10. Using a 5-range sample full width half-max for a 7-range sample pulse indicates that the central 5-range samples of the pulse contains 52 percent of the temporal pulse energy. Therefore, the mean current demand on the entire array, during the 5-range sample central period is 984-mA, assuming 30-percent quantum efficiency. Therefore, during this pulse return, the current demand increased by a factor of 4169 over the dark response level.

The specific voltage regulator could not be identified or removed for testing, but it is unlikely that device will be able to compensate for a 984-mA demand swing in 5-ns, without deviation. Therefore, the supplied reverse bias voltage will vary under optical loading. The time scale of the sampling operation ensures that the transient responses will be present in the data, even though the voltage regulator attempts to maintain a constant reverse bias voltage.

3.5 ROIC Model Details

Each APD in the array is multiplexed to a set of twenty integrating capacitors. During data collection, photo-current and noise current from the APD sequentially charges these capacitors for a period less than the 1.862-ns switching time. Upon demand, the capacitor charges are serially recorded through an amplifier and analog-to-digital converter to system memory as a digital count. The series of digital counts recorded from the integrating capacitors represents the irradiance on that APD at the time of recording. The spatial composite of all the pixels' records form a frame of data.

For each frame of sular mode data, a laser pulse is triggered and a detector at the laser's aperture monitors the actual pulse output from the laser. When the output is detected, the LADAR's internal clock begins cycling and the detector array is activated and begins cyclically over-writing its capacitor charges. Once a time delay corresponding to the selected range has elapsed, the detector array is deactivated and the integrating capacitor values are recorded to memory introducing readout noise [2].

The amplifier and A/D conversion process produce current values whose units are not in terms of photo-electrons, due to the various scaling factors. For specific amplifier and reference reverse bias voltage settings, the system can be calibrated against a known radiometric source to produce true photo-electron counts. The gain variation phenomenon significantly complicates this calibration procedure. Fortunately, having this exact relationship is not necessary for ranging.

3.6 Model Implications

The first major implication of the proposed system model is nonlinearity. If one record is taken under ambient lighting conditions, a certain photonic load is induced on the system, and the reverse bias voltage varies. If a second record is taken at a brighter ambient condition, a greater photonic load is incident, and the reverse bias voltage varies in a different fashion. Since Miller's equation is nonlinear with respect to reverse bias voltage, the difference between the two records is not the linear difference of the incident light levels. Even dark current subtraction must be treated with caution, because the dark current is also a function of the APD gain. However, with incident photons only due to self emission of the optics and a lens cap, it is the most linear signal which can be measured under field conditions.

For any ranging situation of interest in a military application, there are always at least two inputs. The ambient light from the scene sets the reverse bias voltage, and thus the gain, in motion prior to any returning laser pulse's arrival. Even if the gain behavior during the pulse's arrival is completely dominated by the detector's response to the pulse, the initial gain value is not constant in range. Therefore, the system's response to the laser pulse is not shift-invariant.

The resulting nonlinear time-variant ranging response complicates both data processing and ranging. If the dark response is taken as a linear value, it can be subtracted from a pulse illuminated response, in order to remove additive fixed pattern noise, but the ambient response cannot be subtracted. The effects of the system wide gain fluctuation due to optical loading must also be removed from pulse illuminated records, to produce a linear time-invariant signal for range estimation.

3.7 Residual System Identification

A mathematical model is available for the nonlinear average APD gain, and a second-order closed-loop PID model is proposed for the voltage regulator plant. However, no information is available regarding the actual PID parameters of the

voltage regulator or the presumed RC network resulting from the biasing arrangement of the ROIC. Additional effects from the analog-to-digital conversion are intrinsically recorded in the system's output, which must also be removed prior to considering the system's response. Since the system cannot be disassembled to directly measure component responses, a system identification problem remains.

An iterative approach is used to sequentially remove the effects of the ROIC, time variance, and nonlinearity to examine the closed loop relationship between the current demand on the voltage regulator and the reverse bias voltage provided. An impulse response for the voltage regulator is the desired result, if the current demand and bias voltage are known [13]. Once the response of the voltage regulator is known, it can be coupled with Miller's equation and an iterative process to predict the system's response to a known photonic input which can vary in time on a pixel-by-pixel basis.

IV. Model Development and Intermediate Findings

4.1 Introduction

This chapter describes the process of exposing and identifying the underlying voltage regulator behavior, which is responsible for the APD gain variation and time-variant system behavior. Intermediate system response findings are examined, and data analysis process improvements are suggested where appropriate. The experiment is presented in its signal flow order, in this case from the noisy recorded output back to the photon detection process.

4.2 Random Error Suppression

The device manufacturer, ASC, suggests that the dominant random noise source in the system is read-out noise, which is typically GWAN [2]. This assertion is supported by the 537-Mhz sampling rate and associated analog-to-digital conversion process to reach 200-Hz image sampling across the array [1]. This random noise distribution can be observed without consideration of the proposed nonlinear time-variant model.

The probability distribution shown in Figure 4.1 is derived from the presumption that the mean of one hundred records of the same range slice represents the true image, and deviations from this value at each pixel represent random noise. Since this frame is an actual laser pulse return, it is expected to have a contribution from the Poisson photonic detection process and the GWAN digitization and read-out process [1]. While this distribution is not a perfect fit to a Gaussian, the Gaussian form appears to dominate the noise behavior. Were this not the case, the symmetry of the distribution would be further distorted, unless the Poisson lambda value exactly equalled the mean GWAN value.

Multiple frame averaging is used to suppress the random error, from all sources, in the data collected for this work. While other filtering methods are necessary for military applications when the target cannot be imaged multiple times, these are not pertinent to the development of the model. The signal to noise ratio can be improved

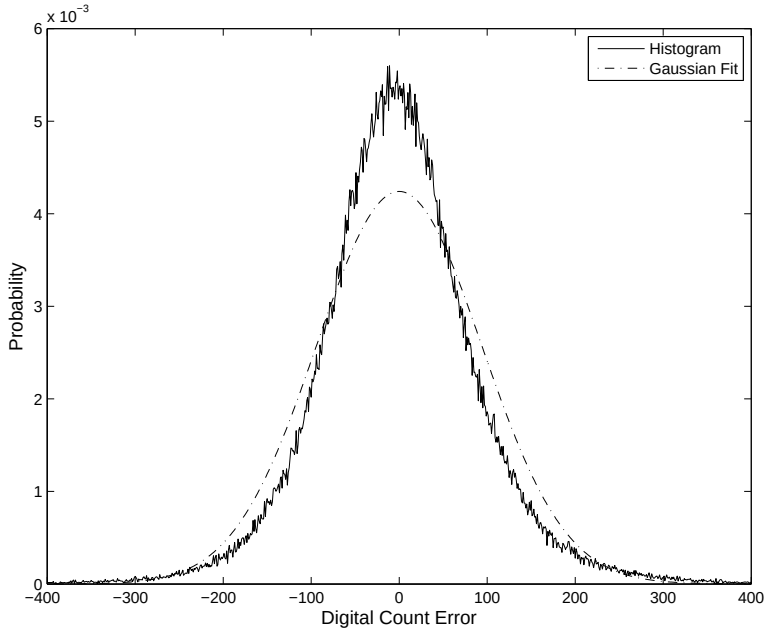

Figure 4.1: Illuminated scene noise distribution

by a factor of ten for signals with GWAN by simply averaging one hundred frames. This amount of averaging appears to suppress random error effects sufficiently to proceed with systematic error suppression.

4.3 ROIC Systematic Error Suppression

The systematic error contribution of the ROIC is generally modeled as a multiplicative gain variation between amplifiers and an additive offset for each amplifier. A multiplicative and additive response is also present due to the individual APDs in the arrays. Because APD responsivity variation is under investigation, amplifier gain variations cannot be evaluated at this stage of the model. However, the additive offset terms can be examined when the APD multiplicative term is acting on a near-zero value.

In order to introduce a minimum of photonic input, a series of frames was taken with the lens cap on the flash LADAR's optical system. Even in this dark condition, some electrons will be released by the APD due to photons from self-emission of the optical components and casing, as well as thermal effects within the APD itself [3].

As previously indicated, the mean individual APD dark current was 14.4-nA prior to read-out amplification for a developmental version of this device [2]. The dark response current demand is as low as it can be made for the system, and the smallest possible gain variation due to optical loading is experienced. Therefore, the results will be attributed to the ROIC as an additive component.

The additive components from the dark response represent fixed pattern noise in the data cube, the values of which vary both by pixel and by range sample. A series of dark response measurements at increasing range delays was taken and the averaged results for one pixel with error bounds are shown in Figure 4.2. The pattern of the recorded value is clearly repeated, but its amplitude increases with increasing range. During the recording time, the incident photons and dark current from the APDs cannot be fluctuating in a consistent enough manner to demonstrate this behavior after averaging. If this was the result of thermal build-up, the responsivity would have decreased as the system warmed up, rather than increased. Further justification for assigning the additive offset values to the ROIC can be found by examining the variance around the mean values. Once again, a relative frequency probability distribution indicative of GWAN is observed in Figure 4.3, with even less symmetry distortion than the illuminated case shown in Figure 4.1.

For the dark response case, the APD gain has been assumed to be as close to constant valued and LTI as it can be in operation in this system. The additive fixed pattern noise attributed to ROIC is also assumed to be the product of an LTI process. Therefore, any illuminated data cube represents a sum of the fixed pattern result and the output of the non-LTI system response under optical loading. If this is so, it is mathematically valid to subtract fixed pattern noise, which never entered a nonlinear process, from an illuminated result.

It is important to note that it is not strictly appropriate to subtract an illuminated data cube from another illuminated cube, such as a record of the same day-lit scene with and without a laser pulse present. When the pulse is active, the laser pulse

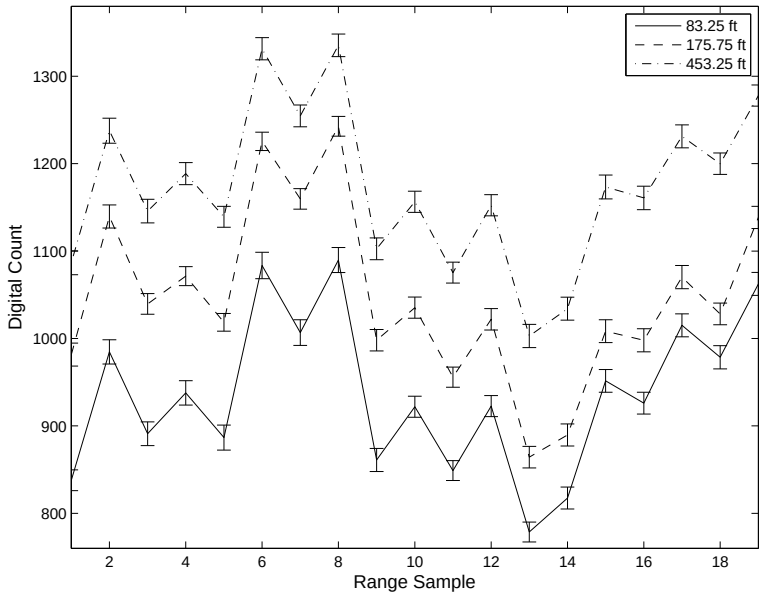

Figure 4.2: Dark response noise structure and standard deviation

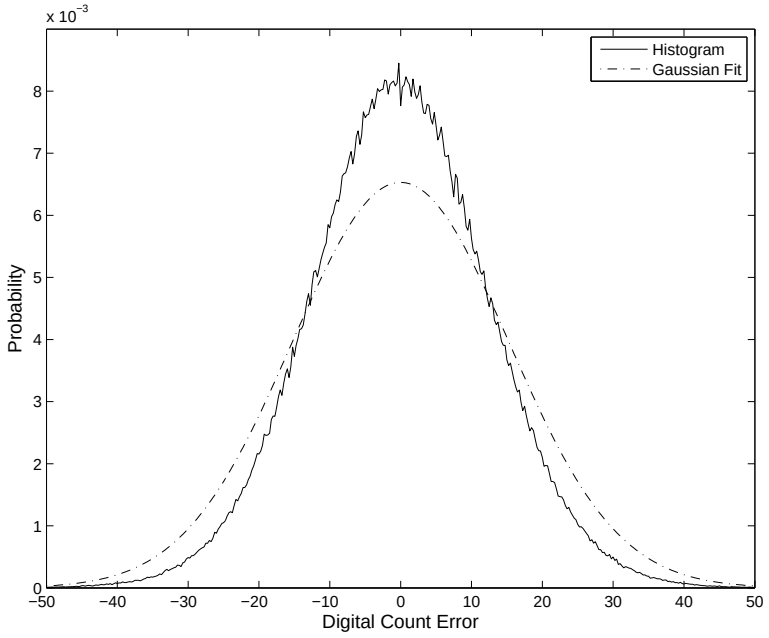

Figure 4.3: Dark response noise distribution

and ambient photons are linearly added before entering the nonlinear time-varying process, then the fixed pattern noise is added to the result. If an ambient data cube is subtracted from a pulse illuminated data cube, the additive pattern noise is removed, but the remaining signal is deformed by subtracting the final results of two nonlinear time-varying processes. Therefore, only dark responses, or ambient responses approaching the dark response, should be directly subtracted from illuminated data to remove additive fixed pattern noise.

4.4 Time Variance

The time variance of the system is the next obstacle to be overcome, in order to examine the voltage regulator response. The proposed model indicates a system which is time variant, in that each pixel contributes to the system's current demand according to when photons are incident upon that pixel. Likewise, the scale of each pixel's contribution to the total current demand depends upon the gain factor, which varies in time according to the total current demand and system response.

Since the time variant response arises from pixels demanding photocurrent at different times, the time variance can be suppressed by exposing the entire array to an input with uniform time varying behavior. A step input across the entire APD array is a simple and direct method of achieving this result. If the APD array is exposed to a constant irradiance, but no reverse bias voltage is applied, no photon driven output response is expected. As soon as bias voltage is applied, the output will begin responding to the irradiance on the detector. Thus, the application of reverse bias voltage effectively generates an approximate step input response from a constant irradiance.

A halogen lamp with a hemispheric reflector was used to provide an approximately constant photon exposure on each pixel. Radiometry indicates that there will be variations in irradiance between pixels due to the physical orientation of the lamp and the flat array [3]. However, with the time variance suppressed, the average response of the APD array to an average irradiance can be determined as if it were

a single time invariant detector. This result allows the system response to be further evaluated.

4.5 Time Concatenation

Figure 4.4 indicates that the APD array is biased at the initial activation for each frame, rather than just prior to recording. Therefore, concatenating successive records can be exploited as a method to record a longer response than a single frame, and provide a much more accurate overall system response measurement. Concatenation is shown not only to be viable, but to indicate another source of systematic error which otherwise would not have been detectable.

A series of fifty-four dark responses at successively increasing range delays and fifty-four corresponding illuminated responses were recorded. One hundred frames were taken for each record and averaged to improve the signal-to-noise ratio. Each dark response record was subtracted from its corresponding illuminated record and the results re-ordered to reflect their proper temporal order.

Each record has an associated start delay distance which is recorded down to one-quarter foot intervals. For alignment, each record was up-sampled by a factor of four and shifted by integer increments to its indicated start location. The results are shown in Figure 4.5.

As expected, each pixel's records did not overlay perfectly, as shown for three records in Figure 4.6. The beginning of each successive record appears to be attenuated compared to the previous record at the same range, but agrees well later in its record. However, the overall form of the overlaid records indicates that concatenation is possible, if a peak value envelope is taken to represent the signal's true form. Beginning with the second record for each pixel, the maximum value of each record was retained in its area of overlap with the following record.

The averaged concatenated record from 1089 pixels near the center of the array was taken to represent the average system response to a step input. This average

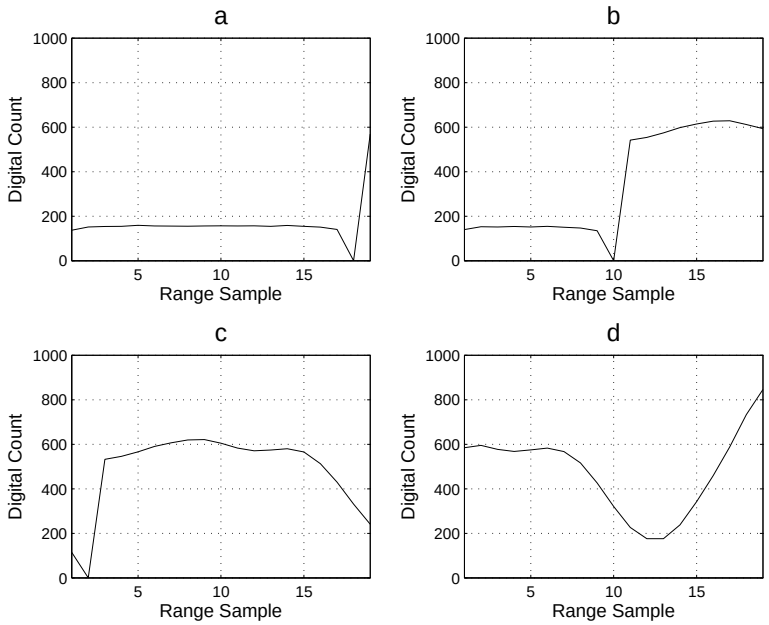

Figure 4.4: Halogen lamp illuminated responses minus dark respones for ranges a. 0-ft b. 9.25-ft c. 18.5-ft d. 27.75-ft

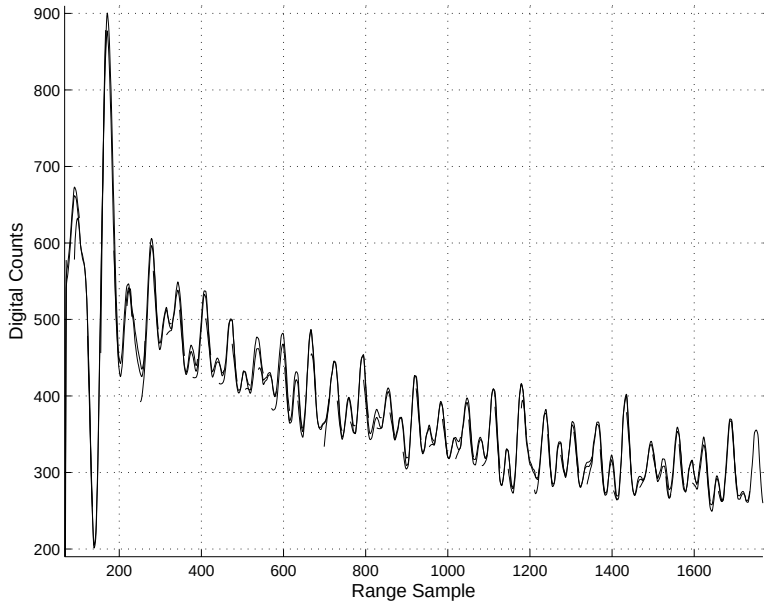

Figure 4.5: Overlay of illuminated conditioned responses for fifty-four ranges.

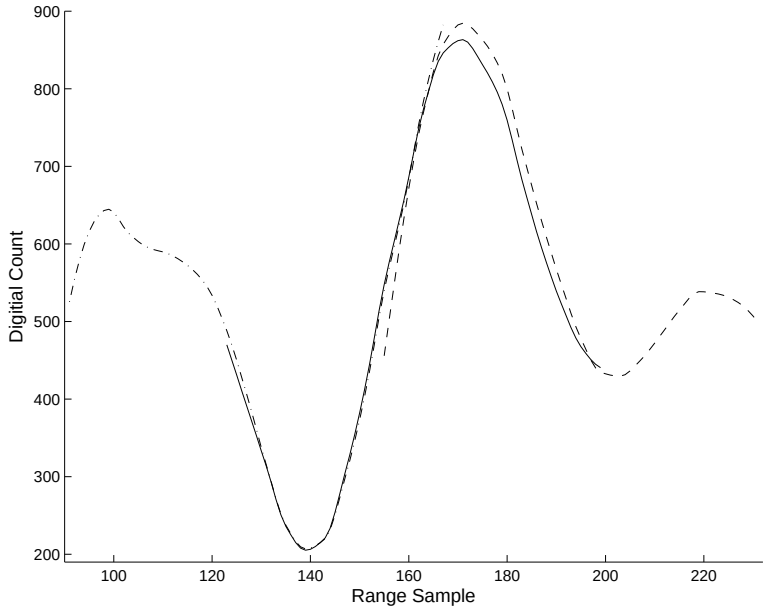

Figure 4.6: Overlay of three conditioned illuminated response records

result, seen in Figure 4.7, shows improved smoothness when compared to individual records, due to the resulting attenuation of any discontinuities in the overlap region specific to one pixel's set of records. After further interpretation, this signal was used to determine the voltage regulator response.

4.6 Overlap Deviation

The consistency of the overlap error between records prompted further examination of the effect. In the absence of concatenation, no indication can be had as to what the expected value at a certain range sample should be. However with the signals concatenated, it is hypothesized that the trailing portion of each record represents the true value. Since additive fixed pattern noise from the ROIC has already been removed, the deviations of the leading portion of the records are hypothesized to be the results of a multiplicative process. Based on this hypothesis, Figure 4.8 shows an average multiplicative correction factor for the overlapping region, as well as the standard deviation associated with this average at each point.

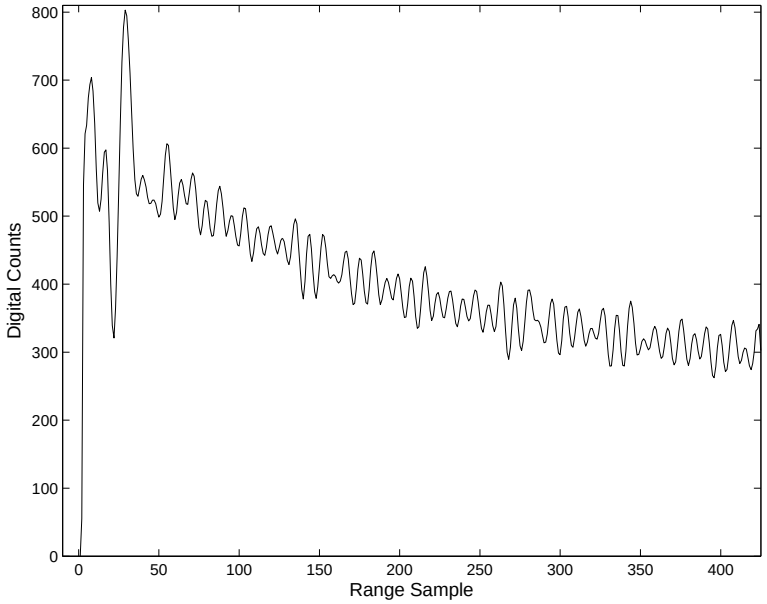

Figure 4.7: Concatenated record maximum value envelope

In light of the dark current's increasing baseline value over time, an analysis of the temporal behavior of the overlap deviation was also conducted. No trend was identified regarding the behavior earlier or later in the sequence, as it was for the recorded dark current values. Rather, the overlap deviations of those range samples which occurred prior to the expected start time of the step-like input were found to have a higher variance and behavior less consistent with the averaged values than range segments which occurred later.

Due to the consistency of this factor through 1089 pixels and 53 overlapping regions, it is recommended that this factor be applied to recorded data even in the absence of record concatenation. If it is not applied, the beginning of a record will be attenuated and any pulse return shape modified by the inverse of the correction factor. This type of deviation will cause most sub-sampling time increment range determination algorithm estimates to indicate an object more distant from the LADAR than its actual range.

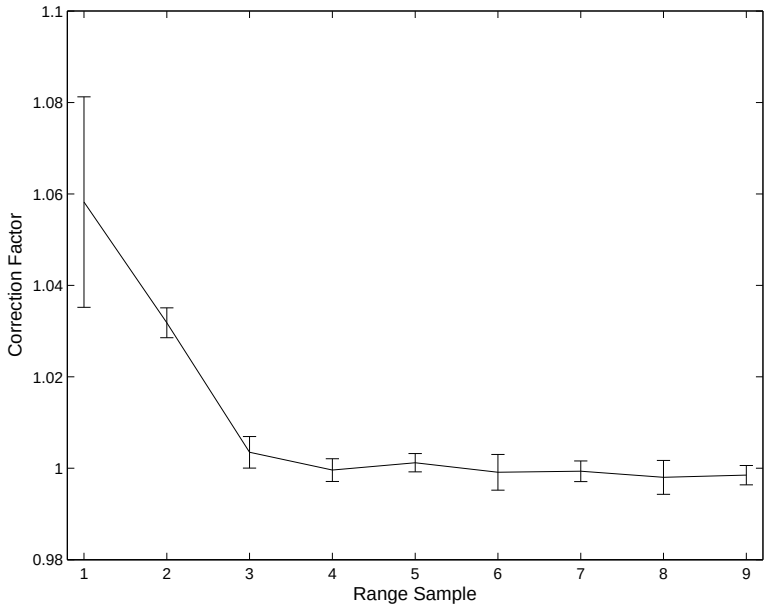

Figure 4.8: Correction factor for overlap with standard deviations

4.7 Time Domain Data Interpretation

Thus far, an output response to an approximate photonic step input has been conditioned and concatenated. This result is re-interpreted to allow the nonlinear process to be removed and find a linear system relationship between the current demand and the reverse bias voltage. The following process was used to determine the reverse bias voltage and current demand during the record.

The output record represents the charge stored in the integrating capacitors after analog-to-digital conversion, and therefore goes as the current demand placed on the voltage regulator. This result is best kept in its unmodified form, because the analog-to-digital converter introduces scaling and includes lower and upper bound limits which can significantly effect how a given capacitor charge is interpreted. It also means that this result must be re-derived if the analog-to-digital conversion settings are changed.

The photon input demand is presumed constant throughout the record, since the detector was illuminated by a lamp rather than a pulse. In accordance with the proposed system model, all of the system feedback is presumed to enter the recorded

output via gain variation. Therefore, if properly scaled, the result shown in Figure 4.7 represents the gain variation in time, when the system is exposed to a photonic step input.

A digital count value must be chosen which represents the system operating at its designed gain value, and several interpretations are possible, depending upon the voltage regulators startup behavior. It is possible that the gain oscillates around the desired value near the end of the record shown in Figure 4.7. It is also possible that the rise time of the voltage was fast enough that the slight knee in the first oscillation at sample two actually represents the desired gain and that the system could not deliver enough current to maintain the desired value in the steady state. Having no compelling evidence at this point for either case, both are retained for evaluation.

If the reverse breakdown voltage for the APDs is consistent and known, equation (3.1) can be solved for the reverse bias voltage. While Sensors Unlimited indicated very consistent reverse breakdown voltages during the development of the APD array, a definitive record of the reverse breakdown voltage of the final device is not available [2]. Lacking this information, the reverse breakdown voltage listed for a developmental device was used as an estimated value.

Both possible reverse bias voltages and both postulated desired gain scaling points were examined. It was found that using the software set value with the desired gain point set at the knee resulted in a modeled reverse bias voltage with an imaginary component, when the gain fell below one. With the reference voltage set one volt below reverse breakdown, the reverse bias voltage model yielded imaginary values when the reverse bias voltage became greater than the reverse breakdown voltage. Therefore, only two of the permutations were evaluated. In the first case, the reverse bias voltage was set one volt below the reverse breakdown voltage, with the gain point set at the knee. In the second case, the reverse bias voltage was set at the software recorded value with the gain point set at the mean of the final two hundred samples considered.

$$V_{Bias} = V_{BD}\left(1 - \frac{1}{G}\right)^{\frac{1}{p}} \tag{4.1}$$

$$V_D = V_{ref} - V_{BD}\left(1 - \frac{1}{G}\right)^{\frac{1}{p}} \tag{4.2}$$

Using the developmental reverse breakdown voltage, equation (3.1) is solved for the reverse bias voltage, as shown in equation (4.1). To strictly indicate the control relationship between the reference, $\mathbf{V_{ref}}$, and the actual reverse bias voltages, the reverse bias voltage is redefined as the reference voltage minus a voltage variation, $\mathbf{V_D}$, in equation (4.2). Each of the postulated gain variation records is then used as an input to equation (4.2) yielding the reverse bias voltage deviation which must have given rise to the recorded gain variation.

After scaling the data to a gain profile, calculating the voltage deviation required to produce that gain, and assigning the current demand to be proportional to the digital count, two signals for each case are available for analysis. The resulting current demand and the reverse bias voltage deviations under consideration are shown in Figure 4.9. These results represent the input and output of the voltage regulator, presumably a linear time invariant system. Any transfer function or difference equation resulting from theses values must be used with a certain caution, because the input signal has limited frequency content. For instance, the high frequency content of an impulse or step response cannot be recreated accurately from these signals. Fortunately, the signals of interest are the convolution of a smoothly varying pulse shape with a target shape which will tend to elongate the return. With this caveat, the signals were used as input and output conditions for a system identification process.

4.8 Linear Constant-Coefficient Difference Equation

Since the input and output signals of the unknown system are discrete, and a significant time history is available, linear constant-coefficient difference equations

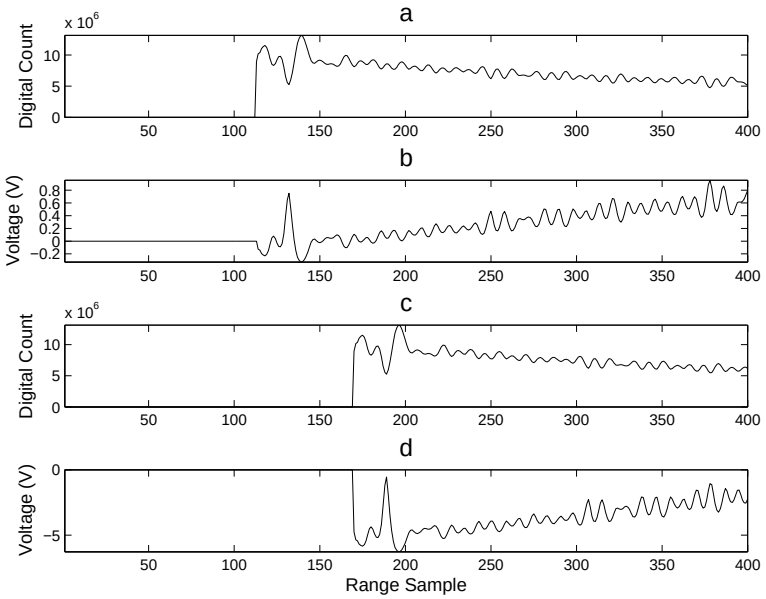

Figure 4.9: a. Case 1 current demand b. Case 1 voltage deviation c. Case 2 current demand d. Case 2 voltage deviation

(LCCDE) can be used for system identification. The difference equations take the form of equation (4.3) where **x** terms are input values and **y** terms are output values at successively delayed indexes. This relationship is solved for equation (4.4) to predict the next output value from a series of known past input and output values [11].

$$x(n) + b_1 x(n-1) + ... + b_q x(n-q) = y(n) + a_0 y(n-1) + ... + a_r y(n-r) \quad (4.3)$$

$$y(n) = x(n) + b_1 x(n-1) + ... + b_q x(n-q) - a_0 y(n-1) - ... - a_r y(n-r) \quad (4.4)$$

An entire set of coefficient values is found by solving a system of LCCDEs relating past known input and output values to predict the current output value using a fixed number of input and output coefficients. Initial conditions, for the system of equations, are taken as zero for the current demand and reverse bias voltage

deviation values. The number of coefficients indicates the overall order of the system. Algebraically, this would lead to a great deal of manipulation for a large number of coefficients.

Linear algebra can be used to simplify the solution by preparing an appended matrix of input terms, output terms and an identity matrix and then finding the reduced row echelon form of the entire matrix [11]. Equation (4.5) shows an example with three input coefficients in $\mathbf{x}$ and two output coefficients in $\mathbf{y}$. The sixth column contains the current output values, in this example.

$$\begin{bmatrix} 0 & 0 & x(1) & 0 & 0 & y(1) & 1 & 0 & 0 & 0 & 0 \\ 0 & x(2) & x(1) & 0 & -y(1) & y(2) & 0 & 1 & 0 & 0 & 0 \\ x(3) & x(2) & x(1) & -y(2) & -y(1) & y(3) & 0 & 0 & 1 & 0 & 0 \\ x(4) & x(3) & x(2) & -y(3) & -y(2) & y(4) & 0 & 0 & 0 & 1 & 0 \\ x(5) & x(4) & x(3) & -y(4) & -y(3) & y(5) & 0 & 0 & 0 & 0 & 1 \end{bmatrix} \tag{4.5}$$

After solving for the reduced row echelon form, the coefficient values for each position are found in the place of the previous current output values. In this example, these values appear in the sixth column. The appended identity matrix now contains the inverse matrix of the input and output values [11]. This result is shown in equation (4.6).

$$\begin{bmatrix} 1 & 0 & 0 & 0 & 0 & b_0 & I_{11} & I_{12} & I_{13} & I_{14} & I_{15} \\ 0 & 1 & 0 & 0 & 0 & b_1 & I_{21} & I_{22} & I_{23} & I_{24} & I_{25} \\ 0 & 0 & 1 & 0 & 0 & b_2 & I_{31} & I_{32} & I_{33} & I_{34} & I_{35} \\ 0 & 0 & 0 & 1 & 0 & a_1 & I_{41} & I_{42} & I_{43} & I_{44} & I_{45} \\ 0 & 0 & 0 & 0 & 1 & a_2 & I_{51} & I_{52} & I_{53} & I_{54} & I_{55} \end{bmatrix} \tag{4.6}$$

4.9 LCCDE Solution

Since the system order is unknown and the solution time for a given matrix is short, an error optimization method was used to determine how many coefficients should be used. The matrix solution was found for one to two-hundred input coefficients and one to two-hundred output coefficients, then the known input values were processed recursively by the derived difference equation. The error between the recorded output voltage signal and the recursively derived output signal was found and recorded. Finally, the set of coefficients which produced the smallest error was selected as the coefficient set for the system model.

The final output system model for Case 1 has ninety input and thirty-nine output coefficients, while the model for Case 2 has one hundred and forty-one input and fifty-five output coefficients. The results of reconstructing the reverse bias voltage deviation records are shown in Figure 4.10.

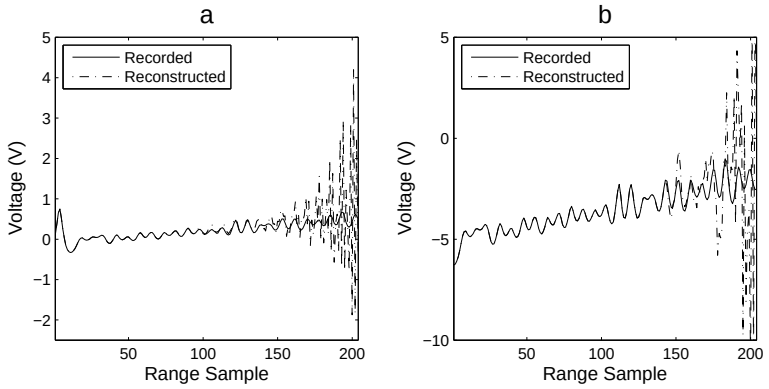

Figure 4.10: a. Reconstructed voltage deviation for case 1 b. Reconstructed voltage deviation for case 2

V. Model Validation

5.1 Forward Process

Based on the system response derived in section 4.9, a direct iterative process is used to predict the result recorded by the system for a known true photon arrival distribution in time, using the following assumptions. First, initial conditions of zero in voltage variation and current demand are assumed for a set of samples as large as the largest number of filter coefficients. Second, the initial gain is presumed to be the empirically derived value for the ideally regulated reverse bias voltage.

The current demand at the time index, **k**, is determined by multiplying the sum of the photon arrival count, $P(q,r,k)$, for each pixel at the time index by the gain, $G(k)$, at the time index.

$$i_D(k) = G(k) \sum_{q=1}^{128} \sum_{r=1}^{128} P(q,r,k) \tag{5.1}$$

Then, the voltage variation for the time index which arises from all previous voltage variations and current demands is recursively calculated using equation (5.2).

$$V_D(k) = I_D(k) + b_1 I_D(k-1) + ... + b_z I_D(k-z) - a_1 V_D(k-1) - ... - a_z V_D(k-z) \tag{5.2}$$

The resulting voltage variation at the time index is then used in equation (3.1) to determine the gain for the next time index. This process is repeated until the known photon arrival values are exhausted, and a gain profile has been calculated for the entire record length. Given that only a forward process is proposed, a limited test case is required for which the true photon arrival distribution is known.

5.2 Forward Simulation

If the system model is valid over its range of assumptions, the best measure of its performance is its ability to recreate the gain variation experienced by a simple test

case. Unfortunately, the test cases available for comparison were limited to data taken on previous collections. Since no cases were available for a single surface occupying the entire FOV, a compromise case was selected. The derived noise reduction procedures were applied to the recorded data and the RGB estimation method was used to determine range values using the original and modified system models.

The test scenario consists of a two-surface target boards, the ground, the ambient lighting conditions, and some foliage near the end of the range record. While not ideal, this data set was taken at night, minimizing the gain variations due to the system's initial step response when exposed to ambient light. The return from the ground and vegetation causes some deviation from the modeled case, and the laser pulse shape is not precisely recorded. An additional obstacle is the lack of a record of the target surface separation or true target range for this data set.

Following the procedure for additive fixed pattern noise removal developed in section 4.5, a dark response measurement for the range delay of the test data set was taken. Both the dark response and recorded data set consisted of one-hundred frames. Therefore, random noise suppression on par with the model development values was achieved through frame averaging. The averaged result of the dark response was subtracted from the averaged illuminated frame to generate the final frame for the ranging algorithm.

The RGB estimation theory method was selected as the ranging algorithm for the test. This selection was due to its simplicity of implementation and relevance to ongoing research. The algorithm was run on the recorded data set in its original form with a resolution of 1/30 of a range sample, or approximately 2-cm, and on the recorded data modified by a varying gain profile at the same resolution. To derive a gain profile, each pair of postulated inverted parabola amplitudes and locations was used as a true photonic input into the non-LTI system model. Thus, the gain profile was different in each iteration, depending upon the hypothesized ranges of the target surfaces.

The photonic scaling for the input parabolas was somewhat arbitrary, being based on previously calculated radiometric values for the target. For the purposes of the model, as long as the photonic pulse amplitude is the correct factor greater than the bias photonic level, the scaling factor in the ranging algorithm will rescale the results to match the digital count record. The photonic bias level was taken from the background recorded mean and the photonic pulse scaled accordingly. Since the front and back surface areas of the test target exposed to the LADAR were of approximately equal area, the total photon input was modeled as the sum of two pulses. This total photon input was run through the forward process described in section 5.1, and the results used to calculate the MSE for each postulated location.

The algorithm was run for both the Case 1 and Case 2 coefficient sets. It was found that using Case 2 coefficients produced an initial voltage variation due to the first surface pulse which generated imaginary gain profile values. Therefore, Case 2 was dropped from consideration. The results for Case 1 are presented in Figure 5.1. It is important to note that, while Case 2 was dropped, the Case 1 coefficients have not been proven to be absolutely correct. Rather, the Case 1 coefficients are shown to be the best model for the actual system response, of those under consideration.

A comparison of the pulse center locations, for Case 1, gives the following results. The unmodified RGB estimation theory method indicated a first surface location of range sample 6.36 and a second surface location of 9.06, based on a minimum MSE of $5.747 * 10^3$-digital counts and $1.755 * 10^4$-digital counts, respectively. The RGB estimation theory algorithm using the proposed system gain model in lieu of the original bias estimation method yields a first surface location of range sample 6.46 and a second surface location of 9.16, with minimum MSEs of $3.922 * 10^3$-digital counts and $5.955 * 10^3$-digital counts. The gain model system results in a factor of 1.465 improvement in the minimum MSE for the first surface, and a factor of 2.946 improvement in the minimum MSE for the second surface.

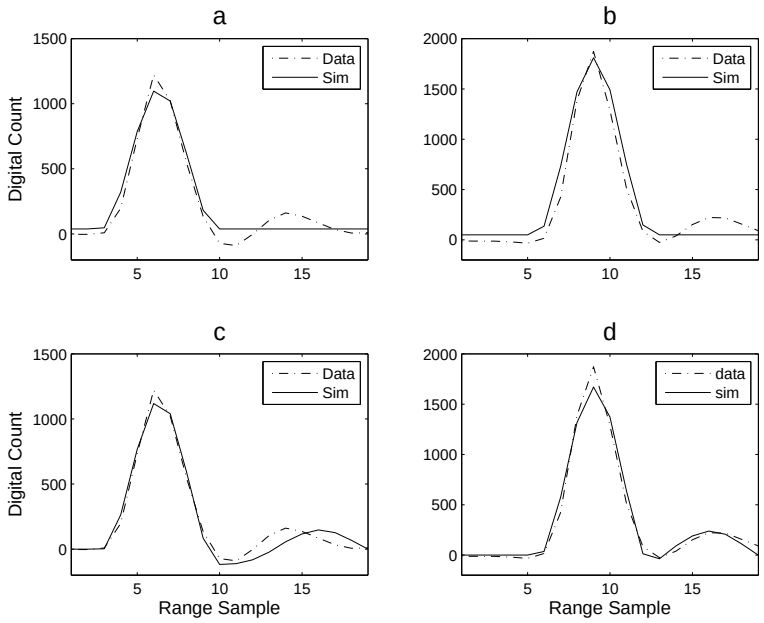

Figure 5.1: a. Original model and data for first surface b. Original model and data for second suface c. Modified model and data for first surface d. Modified model and data for second surface

The results from the modified estimation theory method predict surface locations more distant from the LADAR than the unmodified method. This is in line with the expectation that falling gain as a pulse arrives will tend to skew the pulse center away from the detector. Even handicapped by the inability to postulate the gain variation due to the return from the ground prior to the target, the MSE reductions indicate a significant model improvement. This is particularly true for the second surface, for which the gain behavior can be reasonably expected to be dominated by the first surface return's effects. Pulse reshaping is also evident in the closer fit of the corrected pulse shape to the measured data, when compared to the uncorrected pulse shape.

This experiment cannot show, due to the lack of an independent range measurement, a definitive improvement in the range estimate for the test case. However, it does show a significant reduction in MSE between the recorded data, and the modeled pulse which determined the range estimate. At a minimum, the resulting

improvement of the fit between the modeled and recorded data indicates the validity of incorporating a varying gain component in the system model.

VI. Conclusion and Recommendations

6.1 Primary Areas of Contribution

The primary contribution of this work is to explain and model the anomylous behavior found in data from the AFLR/SNJM FLASH LADAR as a non-LTI gain variation process. It was determined that background subtraction in illuminated scenes must be used cautiously, due to non-LTI nature of the system. The use of dark current subtraction to remove the additive offset component of each pixel and A/D converter has been proposed as a means to reduce additive fixed pattern noise while introducing minimal error. Finally, a responsivity variation, which is attributed to the read-out amplifier, is identified and characterized.

6.2 Significance of Contribution

The significance of the forward model cannot be understated in regards to sub-sample accuracy range determination algorithms, which are derived for LTI signals. The gain variation introduces dependence between all of the pixels in the array, which was neither expected nor modeled previously. In the face of pixel interdependency due to gain variation and the optical system's PSF, the achievable accuracy and resolution of such algorithms can only approach the analytically derived values in very limited cases.

If multiple range returns are to be interrogated from a single IFOV, the gain variation must be removed. Otherwise, true multiple returns may be obscured by the gain variation, and false secondary returns may be observed. Removing the gain profile will also alleviate false ranges being applied to pixels observing targets outside the range gate.

The modification of the background subtracting scheme represents a significant refinement in the understanding of the system. The proposed dark response method introduces less error than the original illuminated scene method, but does not address the contributions of ambient light. To properly remove the ambient light contribu-

tions, the ambient response must be recorded and linearized before subtraction from a linearized pulse illuminated signal.

The amplitude scaling identified during record concatenation also effects ranging accuracy, by non-uniformly rescaling the recorded returns. If only single records were examined, this deviation would likely have been lumped into APD gain variation rather than identified as a separate source of error.

6.3 Recommendations for Further Work

The first recommended continuation of this experiment relates to the Miller's Formula based APD gain term. The near steady state responsivity for a series of bias voltages should be investigated to refine and scale Miller's Equation for this device, at fixed amplifier settings. This may be accomplished by exposing the detector to a series of known input irradiances and concatenating a series of records at the longest delays allowed by the system. This will allow the worst of the transient gain effects to atrophy, and an average of the oscillating value may be taken as the desired value. Making these measurements will answer with certainty where the gain set point lies at the beginning of the record.

It may be possible to investigate the system's response directly. A laser with a pulse length much shorter than the range sampling time increment can be used to generate an impulse like response. If the input pulse intensity is not too high, the gain variation following the pulse may be visible even in dark conditions without saturation. An extended record can be taken by fixing the laser pulse timing and adding progressively more delay for recording in sular mode.

After refining the gain variation model, the next critical step to be taken is to develop an approach to remove the effects of gain variation from the data. Two methods present themselves. The first would be to directly measure the voltage regulator value during recording. If this value were sampled by the ROIC, a refined Miller's Equation could be used to directly rescale the record. Alternately, an iterative

method could be implemented based on the forward model developed in this work. However, this method would require background and dark measurements of the same scene prior to and including the range of interest and will likely prove impractical for all but research tasks.

Appendix A. Matlab® Code

A.1 Matlab® Code for data Process One

Listing A.1: Process1v1.m

```
%Process1v1.m load .seq data files from a fixed directory located ...
    on
%line 63 and averages the results for the entire array.  It also ...
    calculates
%basic statistics on a limited set controlled by the prange vector...
     in
%[1st row, last row, 1st col, last col] format.  A series of ...
    inputs are
%used to allow for partially corrupted data sets to be used.

clear all; close all; clc;
tic,

%1. preparation for data loading%******************

disp('Process set #1');

N=108; %NUMBER of data files

Frames=100; %number of frames per file

FnT=108; % Total number of files

FnD=54; %Total number of data files.  It is expected to be 1/2 the...
     total since a dark
     %current value is needed for each illuminated file.


gapinit=[0]; %gap in file positions for corrupted files - 0 for ...
    none
gap=[gapinit (gapinit-FnD)]; %overlap gap vector for conditioning ...
    of runs which should not be processed due to later gaps

%adjudicate number of good files
if gapinit~=0;
     FnG=FnT-length(gapinit); %Number of Good files
else
     FnG=FnT;
end;

%selction of pixel range under consideration
%[1st row, last row, first col, last col]
prange=[32 64 32 64];

row=prange(1):prange(2);
col=prange(3):prange(4);

```

```
%initialize the pixel value matrix
Pmat=zeros(length(row)*length(col),2);

count=1;
for n=1:length(row);
    for m=1:length(col);
        Pmat(count,1)=row(n);
        Pmat(count,2)=col(m);
        count=count+1;
    end;
end;

%find the number of pixels under consideration for basic ...
   statistics
temp=size(Pmat);
pixels=temp(1);

%2. Load data for overall operations & segment evaluation
%*******************************************************
for q=1:1:FnT; %incrment through number of files

        if sum(gap==q)~=1; %if not a skip file, load data

        [D,H,stop,mark]=flash_read_seqv2('d:\seal\data 10-2-06\',[...
           'seal100206run' num2str(q) '.seq']);
        disp(num2str(q));

        %initialize matrixes for this file
        Dout(q).data=zeros(128,128,20);
        Dout(q).varMat=zeros(pixels,20);
        Dout(q).meanMat=zeros(pixels,20);
        statdata=zeros(pixels,20,Frames);

        for r=1:1:Frames; %increment through Frames
            Dout(q).data=D(r).data+Dout(q).data;  %add the data ...
               for this frame to a total for this file

            for n=1:1:pixels; %increment through each pixel for ...
               consideration
                for m=1:1:20; %increment thru slices for each ...
                   pixel
                    statdata(n,m,r)=D(r).data(Pmat(n,1),Pmat(n,2),...
                       m); %compile statdata matrix
                end;
            end;
        end;

        Dout(q).data=Dout(q).data./Frames; %find overall data mean...
            matrix
        Dout(q).stop=stop; %record stop distance
        Dout(q).pixels=Pmat; %record map of pixels for close ...
           examination
```

```
        Dout(q).varMat=var( statdata,[],3 ); %calculate variance ...
            for each pixel under consideration down the frames
        Dout(q).meanMat=mean( statdata,3 ); %calculate mean for ...
            each pixel under consderation down the frames

    end;

  pack;
    toc,

end;

%save the output results
save process1data Dout N Frames FnT FnG FnD pixels gap Pmat;
```

A.2 Matlab® Code for data Process Two

Listing A.2: Process2v1.m

```
%for those pixels for which basic statistics have been derived in ...
    process1
%conduct a dark current subtraction and concatenate the values to ...
    form
%a single long data run

clear all; close all; clc;

%show plots or not, 1 to show, 0 to not show
showplots=0;

%load data file
load process1data

%initialize a zeros matrix for each pixel
for m=1:1:pixels;
    p(m).data=zeros(FnG,20);
end;

%load values for each pixel into array
for m=1:1:pixels;
    for n=1:1:FnT;
        if sum(gap==n)<1;
            p(m).data(n,:)=squeeze(Dout(n).data(Pmat(m,1),Pmat(m...
                ,2),:));
        end;
    end;
end;

%determine the stop points of the files
stoplist=zeros(1,FnD);
```

```
for m=1:1:FnD;
    if sum(gap==m)<1;
        %multiply by 4 and round to insure integer values of ...
           sampling of
        %stops
        stoplist(m)=round(Dout(m).stop*4);
    end;
end;

%initialize a zeros matrix for each pixel
for m=1:1:pixels;
    q(m).data=zeros(FnD,20);
end;

%dark current subtractions
for m=1:1:pixels;
    for n=1:FnD;
        if sum(gap==n)<1;
            q(m).data(n,:)=p(m).data(n+54,:)-p(m).data(n,:);
        end;
    end;
end;

clear p;
pack;

%initialize a zeros matrix for each re-ordered pixel
for m=1:1:pixels;
    r(m).data=zeros(FnD,19);
end;

%find the zero point & re-order
for m=1:1:pixels;
    for n=1:FnD;
        if sum(gap==n)<1;
            index=find(q(m).data(n,:)<=1);
            r(m).data(n,1:(20-index))=q(m).data(n,( (index+1):20)...
                );
            r(m).data(n,(20-index+1):(19) )=q(m).data(n,1:(index...
               -1));
        end;
    end;
end;

clear q;
pack;

%initialize a zeros matrix for each pixel preparing for 4x interp
for m=1:1:pixels;
    t(m).data=zeros(FnD,77);
end;
```

```
%interpolate each string so they can be aligned
for m=1:1:pixels;
    for N=1:FnD;
        t(m).data(N,:)=interp1(r(m).data(N,:),[0:.25:19],'pchip');
    end;
end;

%clear r;
pack;

%multiply scale for nanoseconds as a reference
x=(1.862/4).*[stoplist(1):1:stoplist(FnD)];

%initialize a final data set variable
sdata=zeros(FnD,length(x));

for m=1:1:pixels;
    s(m).data=zeros(FnD,length(x));
end;

%concatenate the data sets into one signal
for m=1:1:pixels;
    for n=1:1:FnD;
        if sum(gap==n)<1;
            temp=t(m).data(n,:);
            sdata(n,(stoplist(n)-5*n)+6:1:(stoplist(n)+76-5*n+6) )...
                = temp;
            %some hardcoded factors which should be consistent ...
                with the
            %overlap of contiguous files are present +76, -5* ...
                factor
        end;
        s(m).data=max(sdata(1:FnD,1:length(x)),[],1);

    end;
end;

pack;

if showplots==1;
    %form out the images of the values
    for m=1:1:pixels; %replace with pixels for full run
        figure(1);
        subplot(2,1,1);
        for n=1:1:FnD; %replace with FnD for full run
            hold all;
            if sum(gap==n)<1;
                plot( (stoplist(n)-5*n):1:(stoplist(n)+76-5*n), t(...
                    m).data(n,:) );
            end;
        end;
```

```
            title(['overlays of pixel = ' num2str(m) ' position = ' ...
               num2str(Pmat(m,1)) ',' num2str(Pmat(m,2))]);
            xlabel('samples'); ylabel('photo-electron counts');
            hold off; axis tight; grid on;
            axis([0 1767 0 1200]);

            subplot(2,1,2);
            plot(x,s(m).data); axis tight; grid on;
            title(['concatenation of pixel = ' num2str(m) ' position...
                = ' num2str(Pmat(m,1)) ',' num2str(Pmat(m,2))]);
            xlabel('nanoseconds'); ylabel('photo-electron counts');
            axis([0 912 0 1200]);
            set(1,'Position',[-3 39 1280 915]);

            pause;

            close(1);

        end;

end;

%save process output
save process2data s x t r pixels
```

A.3 *Matlab® Code for data Process Three*

Listing A.3: Process3v1.m

```
%This process is run after a series of data sets are concatenated
clear all; close all; clc;
%determine the impulse response from a composite step response

load process2data

%averaging concatenated data sets

data=zeros(1,length(s(1).data));
for n=1:pixels;
        data=data+s(n).data;
end;
data=data./pixels;

save process3data h data
```

A.4 *Matlab® Code for data ABhderiveknee2*

Listing A.4: ABhderiveknee2.m

```
%control input simulation including inverse filtering operations

clear all; close all; clc;

load process3data;
clear h;

%downsample the data back to the original scale, this will ...
    introduce
%some interpolated values.
data=resample(data,1,4);

%set the input value as being the value after division by
%the initial gain, case #1 in the main document
p=5.48;
Vref=XX; %actual value removed for public release
Vbd=XX;  %actual value removed for public release

%initial gain calculation
M1=1/( 1-abs(Vref/Vbd)^p );

%setting input scale to mean in initial values & initializing gain...
     record
scale=mean(data(2))/M1;
input=[scale*ones(1,426)];

M=data(1:426)./input(1:426);
Mhold=M(2:425); %dropping first artifact value

%Vg is the voltage deviation
Vg=Vref-Vbd.*(1-1./Mhold).^(1/p);

Vghold=Vg;

%Alist=[90:1:92], Blist=[36:1:40] to recreate known values
Alist=[1:1:200];
Blist= [1:1:200];

k=1; %additional sequence delays
q=1;
tic;

%increment through the LCCDE solution in matrix form

for index1=1:1:length(Alist);
    for index2=1:1:length(Blist);

        Acof=Alist(index1);
        Bcof=Blist(index2);

        %the zeros assignment is critical for this method to work
```

```
        %also I_d goes as M, but multiplied back to the data ...
            values &
        %assume that every pixel saw the average for the demand
        Id=[zeros(1,floor(max(Acof,Bcof)+min(Bcof,Acof)/2)) Mhold*...
            scale*(128^2) ];

        Vg=[zeros(1,floor(max(Acof,Bcof)+min(Bcof,Acof)/2)) Vghold...
            ];

        %initialize the matrix to be solved via RREF
        Ms=zeros(Acof+Bcof,2*(Acof+Bcof)+1);
        %assign identity matrix values
        Ms(1:(Acof+Bcof),(Acof+Bcof+2):(2*(Acof+Bcof)+1))=eye(Acof...
            +Bcof,Acof+Bcof);
        count=1;

        %assign previous input & output values
        for n=(k+max(Acof,Bcof)):1:(k+max(Bcof,Acof)+Acof+Bcof-1);
            Ms(count,1:(Acof+Bcof+1))=[Id(n:-1:(n-Bcof+1)) -1*(Vg...
                (( n-1):-1:(n-Acof))) Vg(n)];
            held(count).Ms=Ms;
            count=count+1;
        end;

       %solve the system of equations
        Ns=rref(Ms);

        %extract the coefficients
        B=Ns(1:Bcof,(Acof+Bcof+1));
        A=[Ns((Bcof+1):(Bcof+Acof),(Acof+Bcof+1))']';

        %regenerate the test input from the linear difference ...
            equations
        y2=[Vg(1:Bcof) zeros(1,400)];
        x2=Id;

        %iterative forward solution
        for n=(1+max(Acof,Bcof)):(400);
            y2(n)=sum(x2(n:-1:n-Bcof+1).*B')-sum(y2(n-1:-1:n-Acof)...
                .*A');
        end;

        start=length([Vg(1:Bcof) zeros(1,floor(max(Acof,Bcof)+min(...
            Bcof,Acof)/2))]);

        %error calculations & saving coefficient information
        output(q).error=mean( (y2(start:400)-Vg(start:400)).^2 );
        output(q).A=A;
        output(q).B=B;
        output(q).Acof=Acof;
        output(q).Bcof=Bcof;
```

```
            q=q+1;
 95         disp(num2str(q));
        end;

    end;

100 disp(['estimates = ' num2str(q-1)]);
    toc,

    %prepared all saved results for error evaluation
    evals=zeros(1,length(Alist)*length(Blist));
105 for n=1:1:(q-1);
        evals(n)=output(n).error;
    end;

    %search out minima using built in functions
110 Eindex=find(evals==min(evals));
    est=1;

    %notify the user if more than one minima is found
    if length(Eindex>1);
115     disp(['found ' num2str(length(Eindex)) ' mse mins, displaying ...
            first']);
    end;

    %reload the coefficients for the minimum error set
    A=output(Eindex(est)).A;
120 B=output(Eindex(est)).B;
    Acof=output(Eindex(est)).Acof;
    Bcof=output(Eindex(est)).Bcof;
    mse=output(Eindex(est)).error;

125 %regenerate the reconstruction results for display
    y2=[zeros(1,420)];
    x2=Id;

    for n=(1+max(Acof,Bcof)):(400);
130     y2(n)=sum(x2(n:-1:n-Bcof+1).*B')-sum(y2(n-1:-1:n-Acof).*A');
    end;

    toc,

135 disp('NOTE:  The test input has finite frequency content.');
    disp('the resulting impulse response cannot address high frequency...
        inputs');


    %plotting section
140 %**************************************
    figure(1);
    subplot(2,1,1); plot(Vg(1:400)); axis tight; title('filtered ...
       output');
```

```
    subplot(2,1,2); plot(y2(1:400)); axis tight; title(['recon output ...
       of order A= ' num2str(Acof) ' and B= ' num2str(Bcof)]);

145 figure(2);
    subplot(2,1,1);
    plot( (abs(Vg(1:400)-y2(1:400))),'r-'); axis tight; title('abs ...
       error by point');
    subplot(2,1,2);
    plot(Vg(1:400)); hold all;
150 plot(y2(1:400)); hold off;
    title('overlaid voltage & reconstructed voltage');

    %save data for further use
    save ABvalsknee2 A B Acof Bcof Vg y2 x2
```

A.5 Matlab® Code for data ABhderivemean2

Listing A.5: ABhderivemean2.m

```
    %control input simulation including inverse filtering operations

    clear all; close all; clc;

  5 load process3data;
    clear h;

    %downsample the data back to the original scale, this will ...
       introduce
    %some interpolated values.
 10 data=resample(data,1,4);

    %set the input value as being the value after division by
    %the initial gain, case #1 in the main document
    p=5.48;
 15 Vref=XX; %actual value removed for public release
    Vbd=XX;  %actual value removed for public release

    M1=1/( 1-abs(Vref/Vbd)^p );

 20 %setting scale to mean of final oscillations of samples
    scale=mean(data(350:420))/M1;
    input=[scale*ones(1,426)];

    M=data(1:426)./input(1:426);
 25 Mhold=M(2:425);

    %Vg is the voltage deviation
    Vg=Vref-Vbd.*(1-1./Mhold).^(1/p);

 30 Vghold=Vg;
```

```
%Alist=[137:1:141], Blist=[53:1:57] to recreate known values
Alist=[1:1:200];
Blist= [1:1:200];

k=1; %additional sequence delays
q=1;
tic;

%increment through the LCCDE solution in matrix form

for index1=1:1:length(Alist);
    for index2=1:1:length(Blist);

        Acof=Alist(index1);
        Bcof=Blist(index2);

        %the zeros assignment is critical for this method to work
        %also I_d goes as M, but multiplied back to the data ...
           values &
        %assume that every pixel saw the average for the demand
        Id=[zeros(1,floor(max(Acof,Bcof)+min(Bcof,Acof)/2)) Mhold*...
           scale*(128^2) ];

        Vg=[zeros(1,floor(max(Acof,Bcof)+min(Bcof,Acof)/2)) Vghold...
           ];

        %initialize the matrix to be solved via RREF
        Ms=zeros(Acof+Bcof,2*(Acof+Bcof)+1);
        %assign identity matrix values
        Ms(1:(Acof+Bcof),(Acof+Bcof+2):(2*(Acof+Bcof)+1))=eye(Acof...
           +Bcof,Acof+Bcof);
        count=1;

        %assign previous input & output values
        for n=(k+max(Acof,Bcof)):1:(k+max(Bcof,Acof)+Acof+Bcof-1);
            Ms(count,1:(Acof+Bcof+1))=[Id(n:-1:(n-Bcof+1)) -1*(Vg...
               (( n-1):-1:(n-Acof))) Vg(n)];
            held(count).Ms=Ms;
            count=count+1;
        end;

       %solve the system of equations
        Ns=rref(Ms);

        %extract the coefficients
        B=Ns(1:Bcof,(Acof+Bcof+1));
        A=[Ns((Bcof+1):(Bcof+Acof),(Acof+Bcof+1))']';

        %regenerate the test input from the linear difference ...
           equations
        y2=[Vg(1:Bcof) zeros(1,400)];
        x2=Id;
```

```
            %iterative forward solution
            for n=(1+max(Acof,Bcof)):(400);
                y2(n)=sum(x2(n:-1:n-Bcof+1).*B')-sum(y2(n-1:-1:n-Acof)...
                    .*A');
            end;

            start=length([Vg(1:Bcof) zeros(1,floor(max(Acof,Bcof)+min(...
                Bcof,Acof)/2))]);

            %error calculations & saving coefficient information
            output(q).error=mean( (y2(start:400)-Vg(start:400)).^2 );
            output(q).A=A;
            output(q).B=B;
            output(q).Acof=Acof;
            output(q).Bcof=Bcof;

            q=q+1;
            disp(num2str(q));
        end;

    end;

    disp(['estimates = ' num2str(q-1)]);
    toc,

    %prepared all saved results for error evaluation
    evals=zeros(1,length(Alist)*length(Blist));
    for n=1:1:(q-1);
        evals(n)=output(n).error;
    end;

    %search out minima using built in functions
    Eindex=find(evals==min(evals));
    est=1;

    %notify the user if more than one minima is found
    if length(Eindex>1);
        disp(['found ' num2str(length(Eindex)) ' mse mins, displaying ...
            first']);
    end;

    %reload the coefficients for the minimum error set
    A=output(Eindex(est)).A;
    B=output(Eindex(est)).B;
    Acof=output(Eindex(est)).Acof;
    Bcof=output(Eindex(est)).Bcof;
    mse=output(Eindex(est)).error;

    %regenerate the reconstruction results for display
    y2=[zeros(1,420)];
    x2=Id;
```

```
    for n=(1+max(Acof,Bcof)):(400);
        y2(n)=sum(x2(n:-1:n-Bcof+1).*B')-sum(y2(n-1:-1:n-Acof).*A');
130 end;

    toc,

    disp('NOTE:  The test input has finite frequency content.');
135 disp('the resulting impulse response cannot address high frequency...
        inputs');


    %plotting section
    %*************************************
140 figure(1);
    subplot(2,1,1); plot(Vg(1:400)); axis tight; title('filtered ...
       output');
    subplot(2,1,2); plot(y2(1:400)); axis tight; title(['recon output ...
       of order A= ' num2str(Acof) ' and B= ' num2str(Bcof)]);

    figure(2);
145 subplot(2,1,1);
    plot( (abs(Vg(1:400)-y2(1:400))),'r-'); axis tight; title('abs ...
       error by point');
    subplot(2,1,2);
    plot(Vg(1:400)); hold all;
    plot(y2(1:400)); hold off;
150 title('overlaid voltage & reconstructed voltage');

    %save data for further use
    save ABvalsknee2 A B Acof Bcof Vg y2 x2
```

A.6 Matlab® Code for data simcomperror3.m

Listing A.6: simcomperror3.m

```
    %this process applies the forward model coefficents derived in
    %ABhderiveknee2 to a postulated photonic input for comparison to ...
       the
    %recorded signal & range estimation results using Estimation ...
       Theory

  5 clear all; close all; clc;
    %1. load data for filter & data set
    %*********************************************************

    %this background file was taken at night making it very close to ...
       the dark
 10 %current values which would normally be used.
    [D1,H,stop,mark]=flash_read_seqv2('d:\seal\forward Sim\',['plywood...
        background no subtract2.seq']);
```

```
[D2,H,stop,mark]=flash_read_seqv2('d:\seal\Forward Sim\',['plywood...
    no subtract.seq']);

%initialize zeros matrixes for target and background
Dtarget=zeros(128,128,20);
Dbg=zeros(128,128,20);

%averaging out random noise
for n=1:100;
    Dbg=Dbg+D1(n).data;
    Dtarget=Dtarget+D2(n).data;
end;

Dbg=Dbg./100;
Dtarget=Dtarget./100;

%manually re-ordering the pixels
Dbg2=cat(3,Dbg(:,:,3:20),Dbg(:,:,1));
Dtarget2=cat(3,Dtarget(:,:,3:20),Dtarget(:,:,1));

clear D1 D2 Dbg Dtarget H mark n stop;

%2. Find the minimum MSE for the predicted pulse shape estimating ...
   a perfect
%bias for first surface
%*****************************************************************...


H=210;
h1=105;
h2=104;

firstdata=squeeze(Dtarget2(80,64,:)-Dbg2(80,64,:))';

MSE=zeros(20*180,4);
count=1;

%iteratively search through peak amplitude & pulse center ...
   locations and
%calculate error between signal and estimate.

for n=1:20;
    for m=1:180;

        %bias estimation using all values outside the pulse shape
        bias=mean([firstdata(1:floor((105+m-h1+10)/30)) firstdata(...
           floor((105+m+h1+10)/30):19)]);

        %peak scaling solution
        peak=1000+n*10;
        %scaling hanning window as pulse shape
```

```
            pulse=peak*hanning(H);

            %building the 19 point (currently upsampled) estimate
            firstreturn=bias*ones(1,19*30);
            firstreturn( (105+m-h1):(105+m+h2) )=(pulse')+bias;
            firstdown=downsample(firstreturn,30);

            %calculate error on downsampled estimate compared to ...
               recorded
            %signal
            MSE(count,1)=n;
            MSE(count,2)=m;
            MSE(count,3)=mean( (firstdown-firstdata).^2 );
            MSE(count,4)=bias;
            count=count+1;

        end;
    end;

    %find the minimum MSE value
    index=find(MSE(:,3)==min(MSE(:,3)));

    %pull out these values for comparison and display with the ...
       original signal
    n=MSE(index(1),1);
    m=MSE(index(1),2);
    firstMSE=MSE(index(1),3),
    bias=MSE(index(1),4);

    %generate the estimate
    peak=1000+n*10;
    firstpeak=peak,

    pulse=peak*hanning(H);
    firstreturn=bias*ones(1,19*30);
    firstreturn( (105+m-h1):(105+m+h2) )=(pulse')+bias;

    firstcenter=(105+m+30)/30,

    firstdown=downsample(firstreturn,30);

    %plot the estimate and the recorded signal
    figure(1);
    subplot(2,2,1);
    plot(firstdata,'k:'); hold on;
    plot(firstdown,'k-'); hold off;
    axis([1 19 -200 1500]);
    title('first surface MSE + bias');
    legend('data','sim');

    %2. Find the minimum MSE for the predicted pulse shape estimating ...
       a perfect
```

```
%bias for the second surface.  The code runs the same except for ...
    scaling
%*****************************************************************...

seconddata=squeeze(Dtarget2(59,67,:)-Dbg2(59,67,:))';

MSE=zeros(20*180,4);
count=1;
for n=1:20;%20
    for m=1:180;%20

        bias=mean([firstdata(1:floor((180+m-h1+10)/30)) firstdata(...
            floor((180+m+h1+10)/30):19)]);

        peak=1750+n*10;
        pulse=peak*hanning(H);
        secondreturn=bias*ones(1,19*30);

        secondreturn( (180+m-h1):(180+m+h2) )=(pulse')+bias;
        seconddown=downsample(secondreturn,30);

        MSE(count,1)=n;
        MSE(count,2)=m;
        MSE(count,3)=mean( (seconddown-seconddata).^2 );
        MSE(count,4)=bias;
        count=count+1;

    end;
end;

index=find(MSE(:,3)==min(MSE(:,3)));
n=MSE(index(1),1);
m=MSE(index(1),2);
secondMSE=MSE(index(1),3),
bias=MSE(index(1),4);

peak=1750+n*10;

secondpeak=peak,
pulse=peak*hanning(H);

secondreturn=bias*ones(1,19*30);
secondreturn( (180+m-h1):(180+m+h2) )=(pulse')+bias;
secondcenter=(180+m+30)/30,
seconddown=downsample(secondreturn,30);

figure(1);
subplot(2,2,2);
plot(seconddata,'k:'); hold on;
plot(seconddown,'k-'); hold off;
```

```
    axis([1 19 -200 2000]);
    title('second surface MSE + bias');
    legend('data','sim');

    drawnow;

    %3. now use the pulse model system for the gain point set at the ...
       knee
    %both pulse positions must be considered to provide the proper ...
       total
    %photonic demand
    %*****************************************************************...


    load ABvalsknee2; clear y2 Vg h;

    p=5.48;
    Vref=XX; %values suppressed for public release
    Vbd=XX; %values suppressed for public release

    bias=(4*10^5); %A value has to be guessed for the photonic input ...
       so that
                   %gain variations outside the pulse can be observed

    clear MSE;
    MSE=zeros(3*3*3*3,6);
    count=1;
    tic;

    %The values for a,b,c,d can be set closer to the calculated ...
       results to
    %display the output quickly a=1:1:3, b=4:1:6, c=28:1:30, d...
       =34:1:36;

    for a=1:1:20;
        for b=1:1:20;

            for c=1:1:60;

                for d=1:1:60;

                    %photonic pulse record building the peak values ...
                       are based
                    %on quick radiometric calculations, but their ...
                       values are
                    %arbitary as long as they are large enough to ...
                       excite the
                    %gain variation process.  The rescaling of the ...
                       algorithm
                    %will match up to the recorded results if its ...
                       relatively close.
```

```
peak1=160000;
pulse1=peak1*hanning(H)';

peak2=160000;
pulse2=peak2*hanning(H)';

photonstemp1=zeros(1,19*30);
photonstemp2=zeros(1,19*30);
photonstemp1( (105+c-h1):(105+c+h2) )=pulse1;
photonstemp2( (180+d-h1):(180+d+h2) )=pulse2;

%compiling the photonic record
photons=[[zeros(1,120) downsample(photonstemp1,30)...
    zeros(1,41)];
    [zeros(1,120) downsample(photonstemp2,30) ...
       zeros(1,41)]];

%initialize the gain value - only one for the ...
   array
M=[(1./( 1-((Vref-0)./Vbd).^p )).*ones(1,180)];

%initialize a Vg & ID value for each pixel
Vg=zeros(1,180);
Id=zeros(1,180);

%iteratively calculate the gain value due to ...
   photonic
%interaction.
for n=(1+max(Acof,Bcof)):1:(180);
    Id(n)=sum(M(n).*photons(:,n),1);

    Vg(n)=(sum(Id(n:-1:n-Bcof+1).*B')-sum(Vg(n...
       -1:-1:n-Acof).*A'));
    M(n+1)=(1./( 1-((abs(Vref+Vg(n))))./Vbd).^p ))...
       ; %M is based on Vbias
end;

%before adjudicating the gain, we'll add the ...
   background level so it gets
%modified assuming an otherwise flat BG
for n=1:2;
    Pcount(n,:)=(photons(n,:)+bias).*M(1:180);
end;

%rescale these photcounts to digital counts this ...
   section
%also helps reduce the required accuracy of the ...
   photonic
%peak value estimates
Mval=(1./( 1-((Vref-0)./Vbd).^p ));

firstdown=Pcount(1,120:138)-bias*Mval;
```

```
                    firstdown=(1160+a*10)*firstdown/(peak1*Mval);

                    seconddown=Pcount(2,120:138)-bias*Mval;
                    seconddown=(1850+b*10)*seconddown/(peak2*Mval);

                    %calculate and store the MSEs for each estimated ...
                        pulse
                    %position after applying the gain variation ...
                        process
                    MSE(count,1)=a;
                    MSE(count,2)=b;
                    MSE(count,3)=c;
                    MSE(count,4)=d;
                    MSE(count,5)=mean( (firstdata-firstdown).^2 );
                    MSE(count,6)=mean( (seconddata-seconddown).^2 );

                    count=count+1;

                end;

            end;

        end;

    end;

    toc,

    %find the minimum MSEs for the gain variationmodel
    index1=find( MSE(:,5)==min(MSE(:,5)) );
    index2=find( MSE(:,6)==min(MSE(:,6)) );

    index1=index1(1);
    index2=index2(1);

    %combined best values to try to find a common result
    %plotting the minimums for the second best fit

    a=MSE(index1,1);
    b=MSE(index2,2);
    c=MSE(index1,3);
    d=MSE(index2,4);

    %regenerate the results for display
    peak1=160000;
    pulse1=peak1*hanning(H)';

    peak2=160000;
    pulse2=peak2*hanning(H)';

    photonstemp1=zeros(1,19*30);
```

```
photonstemp2=zeros(1,19*30);
photonstemp1( (105+c-h1):(105+c+h2) )=pulse1;
photonstemp2( (180+d-h1):(180+d+h2) )=pulse2;

firstcenter2=(105+c+60)/30,
secondcenter2=(180+d+60)/30,

photons=[[zeros(1,120) downsample(photonstemp1,30) zeros(1,41)];
    [zeros(1,120) downsample(photonstemp2,30) zeros(1,41)]];

%initialize the gain value - only one for the array
M=[(1./( 1-((Vref-0)./Vbd).^p )).*ones(1,180)];

%initialize a Vg & ID value for each pixel 140
Vg=zeros(1,180);
Id=zeros(1,180);

for n=(1+max(Acof,Bcof)):1:(180);
    Id(n)=sum(M(n).*photons(:,n),1);

    Vg(n)=(sum(Id(n:-1:n-Bcof+1).*B')-sum(Vg(n-1:-1:n-Acof).*A'));
    M(n+1)=(1./( 1-((abs(Vref+Vg(n))))./Vbd).^p )); %M is based on ...
       Vbias
end;

%before adjudicating the gain, we'll add the background level so ...
   it gets
%modified assuming an otherwise flat BG
for n=1:2;
    Pcount(n,:)=(photons(n,:)+bias).*M(1:180);
end;

%rescale these photcounts to digital counts

Mval=(1./( 1-((Vref-0)./Vbd).^p ));

firstdown=Pcount(1,120:138)-bias*Mval;
firstdown=(1160+a*10)*firstdown/(peak1*Mval);

seconddown=Pcount(2,120:138)-bias*Mval;
seconddown=(1850+b*10)*seconddown/(peak2*Mval);

firstMSE2=mean( (firstdata-firstdown).^2 );
secondMSE2=mean( (seconddata-seconddown).^2 );

%plot the results for comparison
figure(1);
subplot(2,2,3);
plot(firstdata,'k:'); hold on;
plot(firstdown,'k-'); hold off;
axis([1 19 -200 1500]);
```

```
    legend('data','sim');
    title('first surface MSE + model');

    subplot(2,2,4);
345 plot(seconddata,'k:'); hold on;
    plot(seconddown,'k-'); hold off;
    axis([1 19 -200 2000]);
    legend('data','sim');
    title('first surface MSE + model');
350
    %save the  results
    save simcompresults3;

    print -deps2 simcomperror3.eps;
```

Bibliography

1. Burris, Charles R. *Detection and Ranging of Obscured Targets in 3-D LADAR Data Using Estimation Theory.* Master's thesis, Graduate School of Engineering, Air Force Institute of Technology (AETC), Wright-Patterson AFB OH, March 2006. AFIT/GE/ENG/06-10.

2. Christopher Dries, Wei Huang, Tara Martin and Michael Lange. "InGaAs/InP Avalanche Photodiodes Arrays for Eye Safe Three-dimensional Imaging". *Proceedings of SPIE Vol. 5074 Infrared Technology and Applications XXIX.* The International Society for Optical Engineering (SPIE), The International Society for Optical Engineering (SPIE), Bellingham WA, 2003.

3. Dereniak, E. L. and G. D. Boreman. *Infrared Detectors and Systems.* Wiley Series in Pure and Applied Optics. John Wiley and Sons Inc., New York NY, 1996.

4. Goodman, Joseph W. *Statistical Optics.* Wiley Classics Library Edition. John Wiley and Sons, Inc., New York NY, 2000.

5. Goodman, Joseph W. *Introduction to Fourier Optics.* Roberts and Company Publishers, Englewood CO, third edition, 2005.

6. Hecht, Eugene. *Optics.* Addison Wesley Longman, Inc., Freeport NY, 4th edition, 2002.

7. J. Khoury, J. Lorenzo, C.L. Woods. "Resolution Limits in Imaging LADAR Systems". *Proceedings of SPIE Vol. 5437 Opitcal Pattern Recognition XV.* The International Society for Optical Engineering (SPIE), The International Society for Optical Engineering (SPIE), Bellingham WA, 2004.

8. Jacob, J. Michael. *Industrial Control Electronics, Applications and Design.* Prentice-Hall Inc., Englewood Cliffs NJ, 1998.

9. Jelalian, Albert V. *Laser Radar Systems.* Artech House Inc., Norwood MA, first edition, 1992.

10. Lathi, B. P. *Linear Systems and Signals.* oxford Series in Electrical and Computer Engineering. Oxford University Press, New York NY, second edition, 2005.

11. Lay, David C. *Linear Algebra and its Applications.* Addison Wesley Longman, Inc., Freeport NY, 2nd edition, 1997.

12. Marston, R. M. *Power Control Circuits Manual.* Newnes Circuits Manuals Series. Newnes an Imprint of Butterworth-Heinemann, oxford, England, second edition, 1996.

13. Norton, J. P. *An Introduction to Identification.* Academic Press Inc., New York NY, 1986.

14. Ove Steinvall, Frank Gustaffsson Dietmar Letalick Tomas Chevalier Asa Persson, Hakan Larsson and Pierra Andersson. "Performance of 3-D Laser Radar through Vegetation and Camouflage". *Proceedings of SPIE Vol. 5792 Laser Source and System Technology for Defense and Security*. The International Society for Optical Engineering (SPIE), The International Society for Optical Engineering (SPIE), Bellingham WA, 2005.

15. Stephen Cain, Ernest Armstrong, Richard Richmond. "Deconvolution of Laser Pulse Profiles from 3D LADAR Temporal Returns". *Proceedings of SPIE Vol. 5558 Applications of Digital Image Processing XXVII*. The International Society for Optical Engineering (SPIE), The International Society for Optical Engineering (SPIE), Bellingham WA, 2004.

16. Stephen Cain, Ernest Armstrong, Richard Richmond. "Flash Ladar Range Accuracy Limits for Returns from Single Opaque Surfaces via Cramer-Rao Bounds". *Applied Optics Vol.45 No.24*. Optical Society of America, Optical Society of America, New York NY, 2006.

17. Stettner, Roger and Howard Bailey. "Eye-safe Laser Radar 3-D Imaging". *Proceedings of SPIE Vol. 5412 Laser Radar Technology and Applications IX*. The International Society for Optical Engineering (SPIE), The International Society for Optical Engineering (SPIE), Bellingham WA, 2004.

18. Walter, Michael D. *Deconvolution Analysis of Laser Pulse Profiles from 3-D LADAR*. Master's thesis, Graduate School of Engineering, Air Force Institute of Technology (AETC), Wright-Patterson AFB OH, March 2005. AFIT/GE/ENG/05-22.

19. Zeghbroeck, Bart Van. *Principles of Semiconductor Devices*. University of Colorado at Boulder, Boulder CO, 2004.

REPORT DOCUMENTATION PAGE

Form Approved
OMB No. 0704–0188

1. REPORT DATE *(DD–MM–YYYY)*	2. REPORT TYPE	3. DATES COVERED *(From — To)*
22–03–2007	Master's Thesis	Jun 2006 — Mar 2007

4. TITLE AND SUBTITLE

Nonlinear Time-Variant Response
in an Avalanche Photodiode Array Based
Laser Detection and Ranging System

5a. CONTRACT NUMBER

5b. GRANT NUMBER

5c. PROGRAM ELEMENT NUMBER

6. AUTHOR(S)

Michael D. Seal, Capt, USAF

5d. PROJECT NUMBER

5e. TASK NUMBER

5f. WORK UNIT NUMBER

7. PERFORMING ORGANIZATION NAME(S) AND ADDRESS(ES)

Air Force Institute of Technology (AFIT/EN)
Graduate School of Engineering and Management
2950 Hobson Way
WPAFB OH 45433-7765

8. PERFORMING ORGANIZATION REPORT NUMBER

AFIT/GEO/ENG/07-03

9. SPONSORING / MONITORING AGENCY NAME(S) AND ADDRESS(ES)

Richard Richmond
AFRL/SNJM
3109 P. Street, Bldg 622
Wright-Patterson Air Force Base, OH 45433
DSN: 785-9614

10. SPONSOR/MONITOR'S ACRONYM(S)

11. SPONSOR/MONITOR'S REPORT NUMBER(S)

12. DISTRIBUTION / AVAILABILITY STATEMENT

APPROVED FOR PUBLIC RELEASE; DISTRIBUTION IS UNLIMITED.

13. SUPPLEMENTARY NOTES

14. ABSTRACT

This research effort identifies and models the nonlinear time-variant behavior exhibited by an avalanche photodiode (APD) array based Laser Ranging and Detection (LADAR) system. Based on the original Linear Time-Invariant (LTI) model, the evolution of error in the LADAR signal is examined sequentially from the outgoing pulse through signal digitization. This error evolution shows that the LTI model does not contain a mechanism for causing the observed signal deviations or the failure to meet the Cramer-Rao lower bound for range accuracy. A nonlinear time-variant model is developed based on the interactions of the avalanche photodiodes in the array with the array's voltage regulator. In the refined model, the sum photo-current for the entire array loads the voltage regulator. The resulting reverse bias voltage variations cause the responsivity of each APD to vary in a nonlinear fashion. Because each APD in the array's responsivity depends upon the entire array's photonic loading, each individual APD's response is time variant.

15. SUBJECT TERMS

LADAR(LASER DETECTION AND RANGING),AVALANCHE PHOTODIOES, FOCAL PLANE ARRAYS, VOLTAGE REGULATION

16. SECURITY CLASSIFICATION OF:			17. LIMITATION OF ABSTRACT	18. NUMBER OF PAGES	19a. NAME OF RESPONSIBLE PERSON
a. REPORT	b. ABSTRACT	c. THIS PAGE			Stephen C. Cain
U	U	U	UU	85	19b. TELEPHONE NUMBER *(include area code)* (937) 255–3636, ext 4716